







Preserved landscapes underneath the Antarctic Ice Sheet reveal the geomorphological history of Jutulstraumen Basin

Steven Franke¹  | Hannes Eisermann¹  | Wilfried Jokat^{1,2}  |
 Graeme Eagles¹  | Jölund Asseng¹ | Heinrich Miller¹  | Daniel Steinhage¹  |
 Veit Helm¹  | Olaf Eisen^{1,2}  | Daniela Jansen¹ 

¹Alfred Wegener Institute, Helmholtz Centre for Polar and Marine Research, Bremerhaven, Germany

²Department of Geosciences, University of Bremen, Bremen, Germany

Correspondence to:

Steven Franke, Alfred Wegener Institute, Helmholtz Centre for Polar and Marine Research, Am Alten Hafen 26, 27568 Bremerhaven, Germany.
 Email: steven.franke@awi.de

Abstract

The landscape of Antarctica, hidden beneath kilometre-thick ice in most places, has been shaped by the interactions between tectonic and erosional processes. The flow dynamics of the thick ice cover deepened pre-formed topographic depressions by glacial erosion, but also preserved the subglacial landscapes in regions with moderate to slow ice flow. Mapping the spatial variability of these structures provides the basis for reconstruction of the evolution of subglacial morphology. This study focuses on the Jutulstraumen Glacier drainage system in Dronning Maud Land, East Antarctica. The Jutulstraumen Glacier reaches the ocean via the Jutulstraumen Graben, which is the only significant passage for draining the East Antarctic Ice Sheet through the western part of the Dronning Maud Land mountain chain. We acquired new bed topography data during an airborne radar campaign in the region upstream of the Jutulstraumen Graben to characterise the source area of the glacier. The new data show a deep relief to be generally under-represented in available bed topography compilations. Our analysis of the bed topography, valley characteristics and bed roughness leads to the conclusion that much more of the alpine landscape that would have formed prior to the Antarctic Ice Sheet is preserved than previously anticipated. We identify an active and deeply eroded U-shaped valley network next to largely preserved passive fluvial and glacial modified landscapes. Based on the landscape classification, we reconstruct the temporal sequence by which ice flow modified the topography since the beginning of the glaciation of Antarctica.

KEYWORDS

basal roughness, bed topography, Dronning Maud Land, East Antarctica, erosion, Jutulstraumen Glacier, radio-echo sounding, subglacial morphology, valley geometry

1 | INTRODUCTION

The geomorphology of the subglacial landscape beneath the Antarctic Ice Sheet (AIS) is an essential part to our understanding of its future stability (Sugden & Jamieson, 2018). The bed topography has been modified by extensive glacial and subglacial erosion on continental, regional and local scales (Jamieson et al., 2010). However, large ice sheets do not only erode the bed, but also preserve the subglacial environment in certain regions at the same time, depending on the

flow velocity of ice, and on whether or not the ice sheet is frozen to the ground or sliding (Jamieson et al., 2014). In order to reconstruct the landscape evolution of the AIS, we thus need to understand present and former ice-stream activity and ice-sheet configurations (Siegert et al., 2005) since the glaciation of Antarctica. The reconstruction of the pre-glacial landscape and the determination of regions where the traces of former ice-flow activity are preserved helps to discriminate where glaciers have built up in the past (Sugden & Jamieson, 2018). To do this, we can refer to an increasing amount of

This is an open access article under the terms of the Creative Commons Attribution License, which permits use, distribution and reproduction in any medium, provided the original work is properly cited.

© 2021 The Authors. *Earth Surface Processes and Landforms* published by John Wiley & Sons Ltd.

radar data to map the ice-sheet base and examine the large-scale topography (km scale; e.g., Cui et al., 2020; Fretwell et al., 2013; Morlighem et al., 2020) and individual landforms (King et al., 2009). Depending on the nature and scale of the structures investigated, this needs to be done at high spatial resolution in some locations (tens to hundreds of metres; e.g., Cui et al., 2020; Holschuh et al., 2020; King et al., 2009).

The pre-glacial topography steers ice flow and determines the distribution of selective erosion (Jamieson et al., 2014). Hence, to study the behaviour of the AIS, we depend on an understanding of the relationship between pre-glacial landscapes and the processes by which ice flow can modify them (Jamieson et al., 2014). It is necessary and important to understand this feedback mechanism if we are to improve our knowledge on the past and future ice-sheet behaviour (Jamieson et al., 2010; Oerlemans, 2010). In particular, constraints on ice-sheet and landscape development are key boundary conditions for numerical simulations of geomorphological development of the landscape beneath the AIS (Jamieson et al., 2010).

In this study, we use existing and new high-resolution airborne radar data to improve our understanding of the bed topography and landscape evolution in the source region of the Jutulstraumen Glacier (JG) in western Dronning Maud Land (DML; see Figure 1). JG is the largest and most important outlet glacier in DML (Callens et al., 2014; Høydal, 1996) and feeds the second largest ice shelf (Fimbul Ice Shelf) in DML (Rignot et al., 2013). We present various geomorphological structures at the glacier bed, and interpret them in terms of the regional erosional history. Our results give insight into the effects of past and present ice dynamics on the glacier bed and into landscape development in glaciated areas in general.

1.1 | Regional setting

The present thick ice-sheet cover in DML inhibits a detailed understanding of its geological history since Precambrian times. Only the combination of geological sampling of the sparse outcrops/nuntaks (Jacobs et al., 1998, 2017) combined with aerogeophysical data (Mieth & Jokat, 2014) made it possible to retrieve some first-order information of the regional geology (Figure 2).

These investigations indicate numerous geological affinities between DML and South Africa. Both fragments re-collided between 650 and 500 million years ago (Jacobs & Thomas, 2004) along the East Africa–Antarctic Orogen to form a new southern supercontinent named Gondwana. Massive volcanism started around 180 million years ago both in East Africa and in DML (Elliot, 1992), which finally led to the fragmentation of Gondwana (Jokat et al., 2003; Leinweber & Jokat, 2012; Mueller & Jokat, 2019).

The Jutulstraumen Graben represents a deep topographic depression which cuts through the otherwise continuous DML mountains extending for 1500 km from 15° W to 30° E (Jacobs, 1991; Jacobs et al., 1992). This mountain chain includes the Borgmassivet and Sverdrupfjella, which form the flanks of the Jutulstraumen Graben, and the Kirwanveggen separating the western Jutul-Penck Graben from the main Jutulstraumen Graben (Riedel et al., 2012; Steinhage et al., 1999) in the east (Figure 1c). Since the graben system runs along several geological units of different ages it is still debated whether the graben formed along a geological

weakness of a failed rift formed prior to the Gondwana break-up (Ferraccioli et al., 2005) or has a different origin. JG and its tributary, the Penck Graben Ice Stream, mainly follow the tectonic lineament (Figure 1b,c), which provides a northward-oriented draining system for the East Antarctic Ice Sheet.

South of the exposed mountain range, DML hosts a complex subglacial landscape. Näslund (2001) proposes a step-by-step genesis, starting with the development of relief by subaerial weathering and erosion by mountain glaciers and river systems resulting in an alpine landscape. Afterwards, erosion of the mountain range by large ice streams is followed by the growth of the East Antarctic Ice Sheet in mid-Miocene times (Holbourn et al., 2005; Shevenell et al., 2004). Further east, between the ice streams that flow around the Sør Rondane Mountains, the plateau inland of the escarpment has been interpreted to preserve features of a pre-existing fluvial landscape (Eagles et al., 2018).

2 | DATA AND METHODS

2.1 | Previous radar surveys

Näslund (2001) presented helicopter-based RES data collected along a 260 km profile across the Jutulstraumen Glacier and from a small area around Jutulsessen Nunatak with about 70 km of data. Näslund (2001) used these prevalent data to reconstruct the long-term landscape development in western and central DML. Around the same time, Steinhage et al. (1999) and Steinhage (2001) gathered more than 50 000 km of airborne RES data in DML as part of the pre-site survey for the European Project for Ice Coring in Antarctica (EPICA). Additional aerogeophysical datasets were acquired in the early 2000s in the Jutulstraumen region (Ferraccioli et al., 2005) and in western DML (Mieth & Jokat, 2014; Riedel et al., 2012). These data have supported detailed interpretations of the geological history of central and western DML, compilations of continental-scale bed topography and subglacial-lake distributions (Huybrechts et al., 2000; Fretwell et al., 2013; Goeller et al., 2016; Morlighem et al., 2020), and targeted studies of bathymetry beneath DML's ice shelves (Eisermann et al., 2020; Smith et al., 2020). To date, however, they have not been used for a regional-scale interpretation of subglacial landscape-forming processes that would complement and update the early interpretations of Näslund (2001).

2.2 | Ice thickness and radar data

For this paper, we add new data from an airborne radar survey in 2018/19 (JURAS-2018). For acquisition, we used AWI's (Alfred Wegener Institute, Helmholtz Centre for Polar and Marine Research) multichannel ultra-wideband (UWB) radar. The UWB system is the improved version of the Multichannel Coherent Radar Depth Sounder (MCoRDS 5) developed at the University of Kansas, Center for Remote Sensing of Ice Sheets (CREGIS; Rodriguez-Morales et al., 2014). The radar system comprises an array of eight antenna elements, which is installed on AWI's *Polar 6* BT-67 aircraft. A detailed description of the instrument is given by Hale et al. (2016) and Rodriguez-Morales et al. (2014).

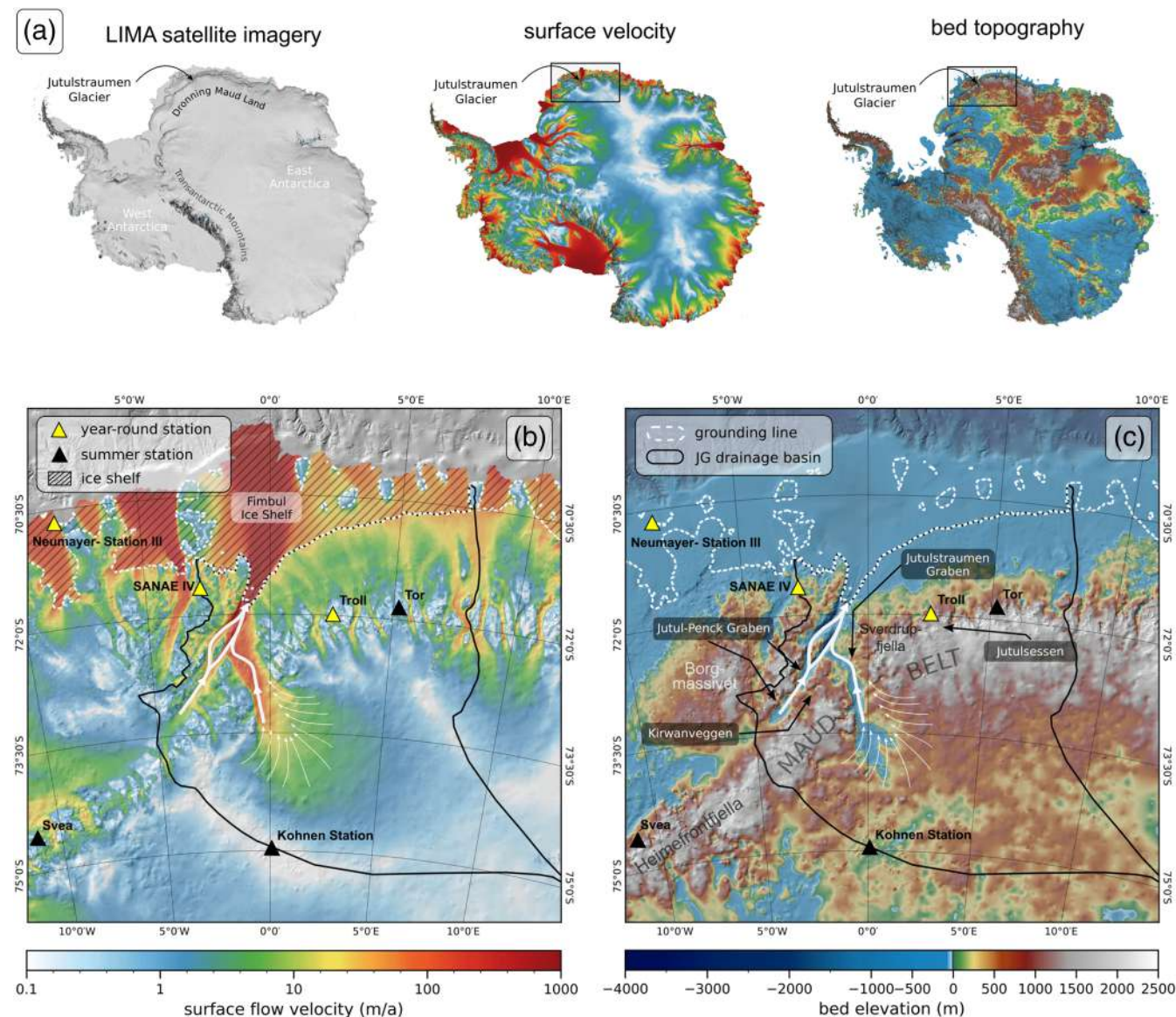


FIGURE 1 Overview of the geographical and glaciological setting of the JG drainage basin. (a) LIMA Landsat image mosaic (Bindschadler et al., 2008), ice-surface velocity (Mouginot et al., 2019) and BedMachine Antarctica (BMA) bed topography (Morlighem et al., 2020). Panels (b) and (c) zoom in on the ice-flow velocity and bed topography maps for the study region. White arrows schematically indicate the convergent ice flow upstream of the Jutulstraumen Graben. The black outline represents the JG drainage system boundary after Mouginot and Rignot (2017). It has to be noted that in our study we focus on the region south of the Maud Belt [Color figure can be viewed at wileyonlinelibrary.com]

All JURAS-2018 radar profiles were recorded in a frequency range of 180–210 MHz and at a flight altitude equivalent to 365 m above ground. For radar data processing, we used the CReSIS Toolbox (CReSIS, 2020). The processing comprises algorithms for pulse compression and Synthetic Aperture Radar (SAR) processing via F-K migration and array processing. Our SAR-processed radargrams have a trace interval of 15 m and a range resolution of 4.3 m. Franke, Jansen, Binder, et al. (2020) give a detailed description of the radar acquisition and processing. The error in calculating the ice thickness is 24.7 m estimated from the RMS of the sum of the crossover mean at 62 intersections. This estimate takes also a 1% error of the dielectric permittivity into account (for further details see Franke, Jansen, Binder, et al., 2020).

The UWB radar data were acquired at the onset of streaming flow, as defined by ice surface velocities of $5\text{--}100\text{ m a}^{-1}$, between the Troll (Norway) and Kohnen (Germany) stations (Figure 3). In the south, the survey covers an area within which ice flow of JG

accelerates. The southern survey lines are oriented perpendicular to the direction of ice flow. The northern survey lines are oriented at $\sim 60^\circ$ to the southern survey lines. They cover parts of the eastern valleys leading to the Jutulstraumen Graben, which also corresponds to an area of accelerating surface velocities and parts of the higher elevated topography to the east of it.

Complementary ice thickness radar data acquired with the AWI EMR (Electromagnetic Reflection System) radar (Nixdorf et al., 1999) and also depicted in Figure 3 were gathered over the last three decades throughout DML (see the section about previous radar surveys and Steinhage et al., 1999, Steinhage, 2001, and Riedel et al., 2012). The profiles of the JURAS-2018 survey were designed to map the ice-bed interface at high resolution while also filling substantial gaps in the existing RES data. Most of these data gaps occur over deep topographic depressions in which the bed could not be detected by older radar systems.

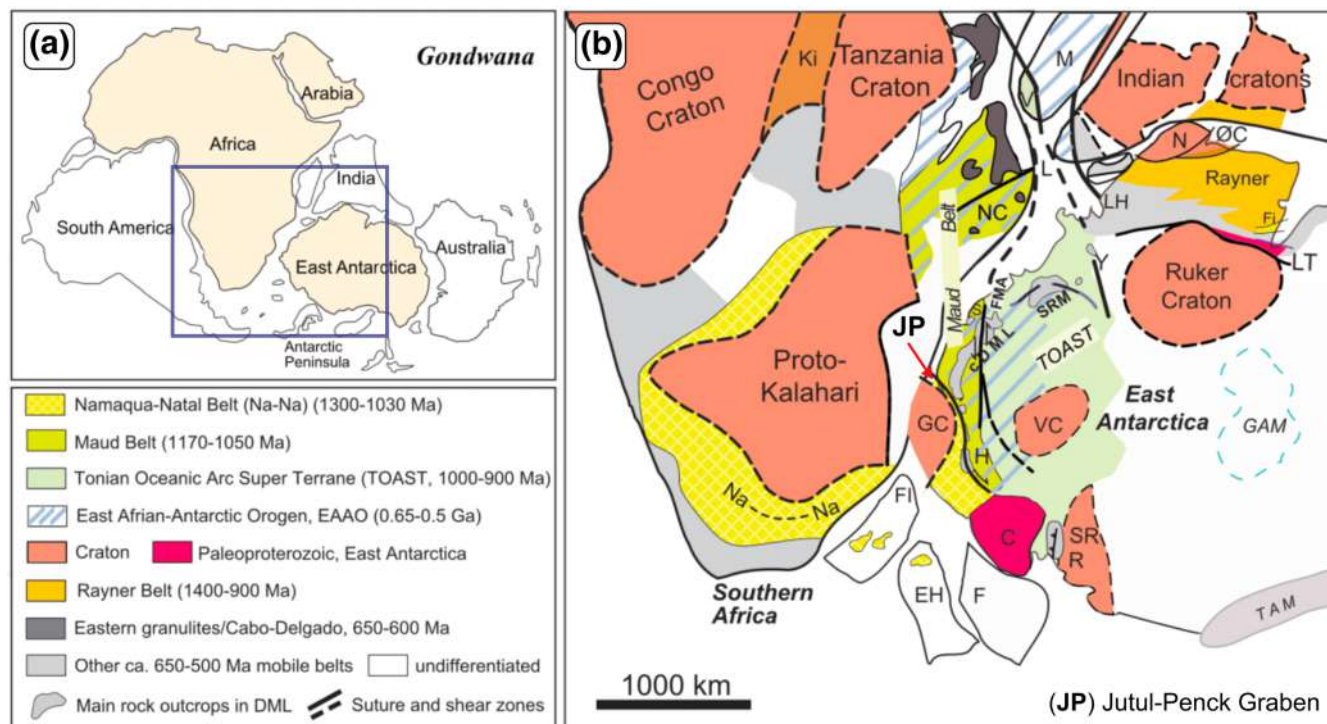


FIGURE 2 Distribution of geological units within Gondwana during Proterozoic and earliest Paleozoic times (Figure modified after Gray et al. (2008), Jacobs et al. (2017), Wang et al. (2020)). The position of DML, East Antarctica is shown in part (a) relative to Africa and India. DML terrane boundaries in part (b) are interpreted from scattered outcrops and interpolated on the basis of regional aeromagnetic data (Jacobs et al., 2017; Mieth & Jokat, 2014). Abbreviations: C, Coats Land; cDML, central Dronning Maud Land; EH, Ellsworth-Haag block; F, Filchner block; FI, Falkland Islands; Fi, Fisher Terrane; FMA, Forster Magnetic Anomaly; GAM, Gamburtsev Mountains; GC, Grunehogna Craton; H, Heimefrontfjella; JP, Jutul-Penck Graben; Ki, Kibaran; L, Lurio Belt; LH, Lützow-Holm Bay; LT, Lambert Terrane; M, Madagascar; N, Napier Complex; NC, Nampula Complex; Na-Na, Namaqua-Natal Belt; ØC, Øygarden Complex; R, Read Block; S, Schirmacher Oasis; SR, Shackleton Range; SRM, Sør Rondane Mountains; TAM, Transantarctic Mountains; V, Vohibori Terrane; VC, Valkyrie Craton; Y, Yamato Mountains [Color figure can be viewed at wileyonlinelibrary.com]

2.3 | UWB radar ice thickness and bed topography

We determine ice thickness by converting the two-way travel time (TWT) of the radar wave between the ice surface and bed reflection to depth. To do this, we use the depth-dependent electromagnetic wave speed in firn and ice (Winter et al., 2017) with a constant electromagnetic wave speed of $1.689 \times 10^8 \text{ m s}^{-1}$ (corresponding to a relative dielectric permittivity of 3.15). The electromagnetic wave speed is the same as used for synthetic aperture radar (SAR) processing (see Franke, Jansen, Binder, et al., 2020). In addition, we use a firn correction factor of 13 m (Steinhage, 2001). The bed topography is calculated by subtracting the ice thickness from an ice surface digital elevation model (REMA DEM; Howat et al., 2019). For the creation of an improved bed topography, we use the SAGA GIS multi-level B-spline interpolation module (Conrad et al., 2015) where line coverage is dense and ordinary kriging where line coverage is sparse. The grid size of our improved bed topography is 1 km.

2.4 | Valley morphology

Knowledge of the morphology, distribution and spatial orientation of subglacial landforms is important for investigating the ice-sheet dynamic history of glaciated and previously glaciated landscapes. For

this study, we analyse the geometry of single valleys along the JURAS-2018 radar transects to determine the developmental stage for a glacial valley (Hirano & Aniya, 1988). We derive three geometrical parameters to categorise the valley type (see Figure 4a): (i) the valley depth D ($D = Z_{\max} - Z_{\min}$); (ii) the valley ratio R , defined as the ratio between the valley depth D and the width at the valley top W_{top} ($R = D/W_{\text{top}}$); and (iii) the V-index (Zimmer & Gabet, 2018). The V-index is defined as the ratio between the valley cross-sectional area of the valley at a specified height above the valley floor A_x and the cross-sectional area of an ideal V-shaped valley with the same height and valley minimum A_v ($V\text{-index} = (A_x/A_v) - 1$). For our study we use this approach on the lower half of the valley depth to avoid taking into account the irregularities of the valley geometry in the upper part.

Next to the trivial parameter D , we use the parameters R and the V-index to obtain information about the geometry of the valley. The valley ratio factor R informs whether the valley is wide or narrow, whereas the V-index helps to discriminate between U-shaped and V-shaped valleys. Here, we bear in mind that the V-index is a relative measure; that is, negative values ($V\text{-index} < 0$) represent a tight V-shaped valley and positive values ($V\text{-index} > 0$) U-shaped valleys. If the V-index equals zero ($V\text{-index} = 0$), the valley matches the ideal V-shaped valley (see Figure 4b and Zimmer & Gabet, 2018). Because valleys are sometimes not symmetrical, the elevation Z_{\max} refers to the elevation of the lower shoulder to determine the valley depth D and to half of the total valley depth for the V-index.

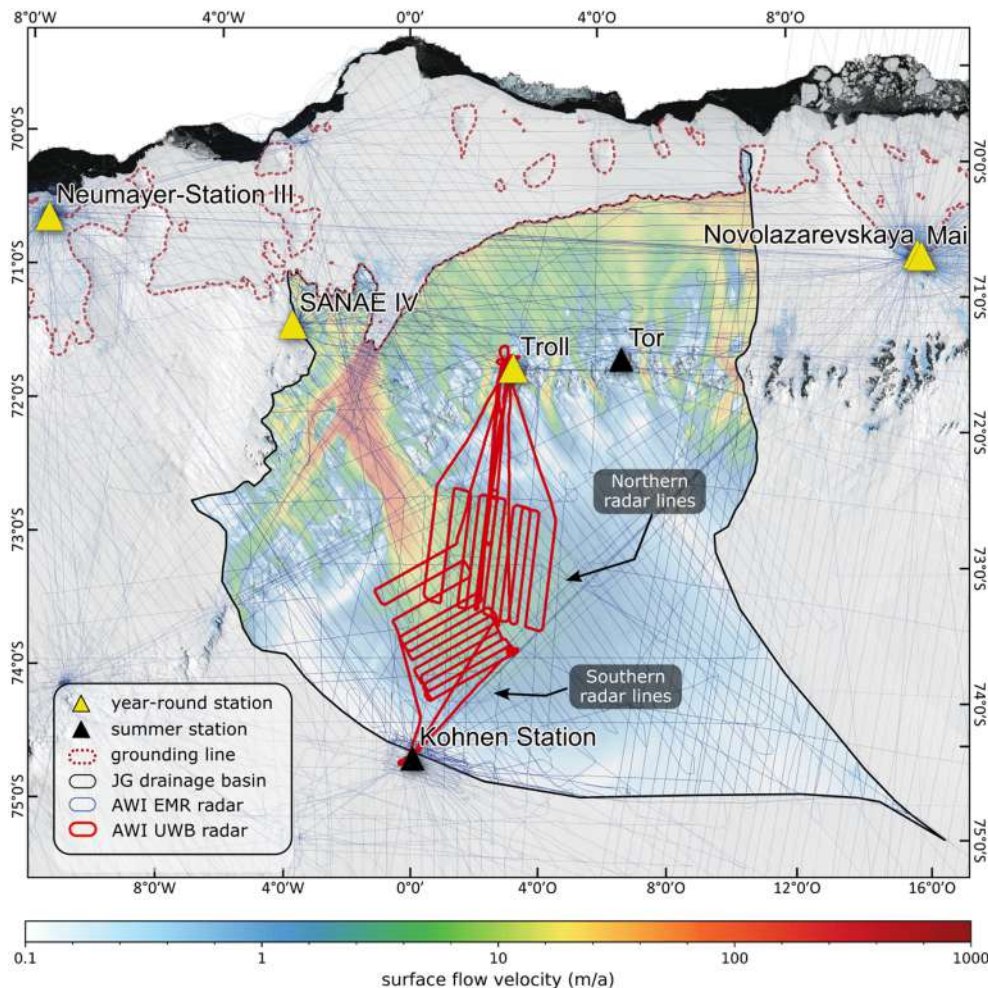


FIGURE 3 Flight tracks with new AWI UWB JURAS-2018 (red) airborne radar data in the Jutulstraumen drainage system (black outline Mougnot & Rignot, 2017). Previous airborne AWI EMR tracks (Steinhage, 2001; Steinhage et al., 1999) are highlighted in blue. Ice-surface velocities (colour code), after Mougnot et al. (2019), are superimposed over the JG catchment. The EPSG projection code for this and all following maps is epsg:3031 [Color figure can be viewed at wileyonlinelibrary.com]

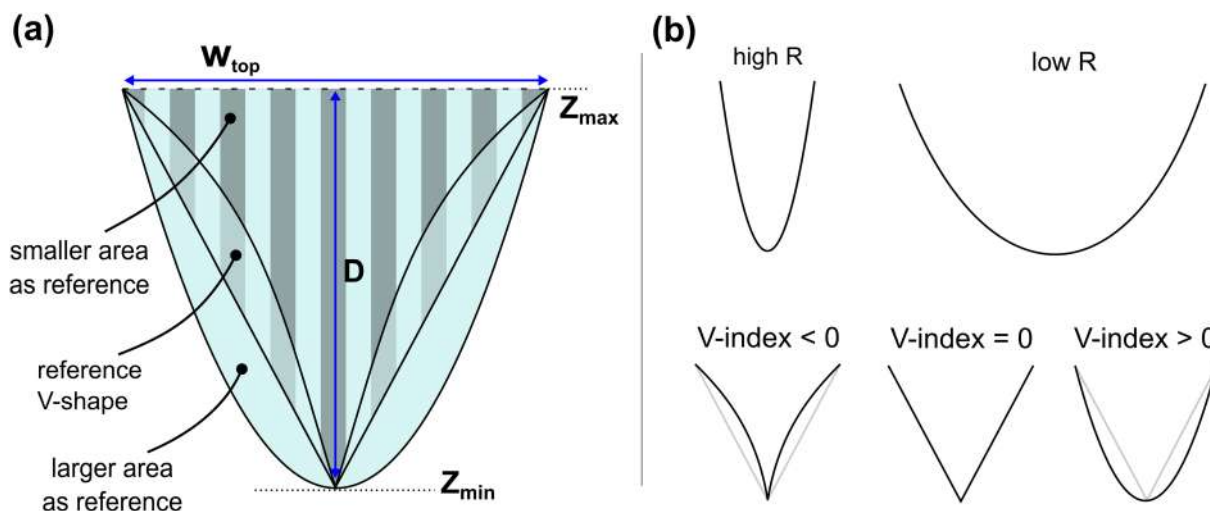


FIGURE 4 Sketch indicating the deviations of parameters used to describe the geometries of valleys. (a) Deviation of the parameters for different valley geometries; (b) resulting valley geometries for the valley ratio R and the V -index [Color figure can be viewed at wileyonlinelibrary.com]

2.5 | Basal roughness

The analysis of valley geometries is somewhat subjective because it relies on a starting interpretation to select the set of features to analyse as valleys. To complement these results, we also analyse basal roughness to quantify the bed topography in a systematic way. Topographic roughness is an indicator of subglacial conditions during

present and past ice-flow activity and a control on current ice-sheet dynamics (Franke et al., 2021; Rippin et al., 2014). Here, we consider a spectral method (Cooper et al., 2019; Li et al., 2010) in combination with the root-mean-square (RMS) height (Shepard et al., 2001) to quantify subglacial roughness.

Spectrally derived roughness is the relative vertical and horizontal variation of the ice-bed interface derived from the nadir bed

reflection. We distinguish between two parameters: ξ , which reflects the vertical irregularity of the bed and provides information about the dominant vertical amplitudes; and η , which describes the dominant horizontal wavelength. For the calculation of these two parameters, we follow Franke et al. (2021). For this study, we use a moving window (MW) length of 512 samples, which corresponds to an approximate ground distance of 7.68 km. We use this value to balance between the detection of large valleys in the roughness analysis as a dominant feature (when the MW is too large) and the fact that valleys may not be detected as roughness when the MW is too small. The majority of radar lines are oriented parallel to each other and approximately perpendicular to ice flow. This alignment promotes a more robust comparison of roughness values than would be possible with a random survey layout.

In addition, we make use of the RMS height. The RMS height χ (or the standard deviation of heights about the mean) is defined by

$$\chi = \left[\frac{1}{n-1} \sum_{i=1}^n (z(x_i) - \bar{z})^2 \right]^{\frac{1}{2}}, \quad (1)$$

where n represents the number of sample points, $z(x_i)$ the height of the bed at position x_i , and \bar{z} the mean height of the detrended profile.

Here, we perform a bed roughness analysis using the JURAS-2018 radar data. The combination of spectral vertical and horizontal roughness estimates enables us to infer the general appearance of the structure at the bed surface, while the RMS height provides information about the absolute elevation differences. The three methods require a uniform sample spacing, which is 15 m in the JURAS-2018 radar data.

2.6 | Isostatic adjustment

We follow the simple approach of Rose et al. (2015) to simulate the isostatic rebound in order to get an idea of the ice-free paleotopography. Here, we only simulate the bed elevation prior to the start of Antarctic glaciation (34 million years ago). The Airy–Heiskanen model (Airy, 1855) predicts that different topographic heights are fully compensated by variations in crustal thickness. We use this model to predict the elevation change the overburden ice will cause on the bed topography. For the calculation, we use densities of 915 kg m^{-3} for ice (ρ_i) 2750 kg m^{-3} for the crust (ρ_c) and 3330 kg m^{-3} for the mantle (ρ_m). For a single location or grid cell, we can calculate the uplift response h_r using

$$h_r = \frac{\rho_c - \rho_i}{\rho_m - \rho_c}. \quad (2)$$

This approach does not account for the entire complexity of processes involved in isostatic rebound after overburden ice removal (Rose et al., 2015). Furthermore, it is possible that the isostatically rebounded topography is underestimated due to erosion and removal of sediment during the last 34 million years, and the original surface may have formed at a higher elevation (Sugden et al., 1995). Nonetheless, we obtain a rough idea about the paleo-topography and are able to use simple statistical methods to infer the characteristics of the landscape.

2.7 | Hypsometry

An isostatically corrected bed topography allows us to analyse the frequency distribution of elevations (hypsometry) to characterise the landscape morphology (Brozović et al., 1997). The aim of this method is to generate indications of whether or not the landscape has a fluvially or a glacially imprinted character. A widespread approach to hypsometry is to create a simple histogram of the frequencies in different elevation bins from a topographic DEM.

In this context, Brocklehurst and Whipple (2004) argue that hypsometry of large arbitrary regions potentially masks the detail in topographic variation in comparison to smaller regions. In addition, hypsometric analyses are sensitive to the resolution of the DEMs on which they are based. The method is most often applied for ice-free alpine regions where the topography is resolved with a grid cell resolution of 30–50 m (Brocklehurst & Whipple, 2004). By contrast, continental-scale bed topography DEMs of ice-covered areas in Antarctica have a resolution of 500–1000 m (e.g., Fretwell et al., 2013; Morlighem et al., 2020) and are interpolated over large distances (up to tens to hundreds of kilometres).

To overcome some of these drawbacks, we follow Creyts et al. (2014) and apply hypsometry on the radar-derived ice thickness data of the JURAS-2018 survey after applying an isostatic correction (Equation 2). For this study, we use the results of a hypsometric analysis to compare different landscapes and to (i) infer the degree of glaciation (Brocklehurst & Whipple, 2004), (ii) discriminate between fluvial and glacial landscapes (Sternai et al., 2011) and (iii) discuss modes of glacial landscape evolution (Jamieson et al., 2014; Li et al., 2010). To avoid a particular sub-region from dominating the signal in the hypsometry, we analyse the entire dataset as well as sub-regions that reflect a particular geomorphological setting.

2.8 | Water flow routing

We apply a simple water flux scheme to simulate the general water flow network, assuming a completely ice-free isostatically compensated topography. By doing so, we aim to approximate features of the paleo-fluvial system in our survey region. We make use of the following SAGA GIS algorithms (Conrad et al., 2015): (i) the *fill sinks* module, to fill surface depressions with a minimum angle of 0.1° and (ii) the *catchment area* algorithm, to calculate the flow accumulation, which represents the number of accumulated cells. In this study, we only perform the water routing for the drainage basin of JG.

3 | RESULTS

3.1 | Radar data and bed topography

The additional ice thickness data of the JURAS-2018 survey allowed us to create an improved bed topography DEM of our survey region (Figure 5). It was possible to fill significant data gaps where the older radar system did not show the bed reflection. However, some data gaps imaging the bedrock topography are still present in the new radar data. The distribution of the gaps is shown in Figure 5b. The majority is located over deep topographic depressions at the onset of

the Jutulstraumen Graben. In the upstream region, data gaps occur in regions with comparable or thinner ice cover than in downstream regions with continuous bed reflections (Figure 6). This indicates that higher englacial attenuation is causing the signal loss or that the bed reflection itself is weaker. Figure 6 shows four JURAS-2018 radar profiles located (a) where the main valley beneath JG is widest, and probably deepest, (b) east of the valleys and (c, d) upstream of the main trunk (profile locations indicated in Figure 5a). Our radar data reveal that the two valleys in the upstream part of radar section D (Figure 6d) merge into the main trunk (Figure 6c). Generally, the bed topography west of the main trunk of JG shows a deeper relief in comparison to the area to the east.

The JURAS-2018 data show regions where the position of the bed is either not interpretable at all or where bottom reflections are too faint for reliable imaging of the full valley geometry (see black dots in Figure 5b and radargrams in Figure 6). Despite these difficulties, it

is still possible to estimate these valleys' general topographies on the basis of the shape of the adjacent bed and internal layering. We use this information in conjunction with the new ice thickness data to create an outline of the valley network associated with the Jutulstraumen Graben (see Figure 5c). A comparison between existing bed topography and new AWI UWB ice thickness data with a subsequent interpretation of the aforementioned data gaps enables the following observations:

1. Gaps occur in both the old and new radar data over pronounced topographic depressions, where no bed reflection could be detected. For some of these regions, the new UWB data added new information.
2. A comparison of JURAS-2018 radar data and the BMA bed shows that BMA generally underestimates ice thicknesses in the JG region, and smooths over the relief of crests and valleys.

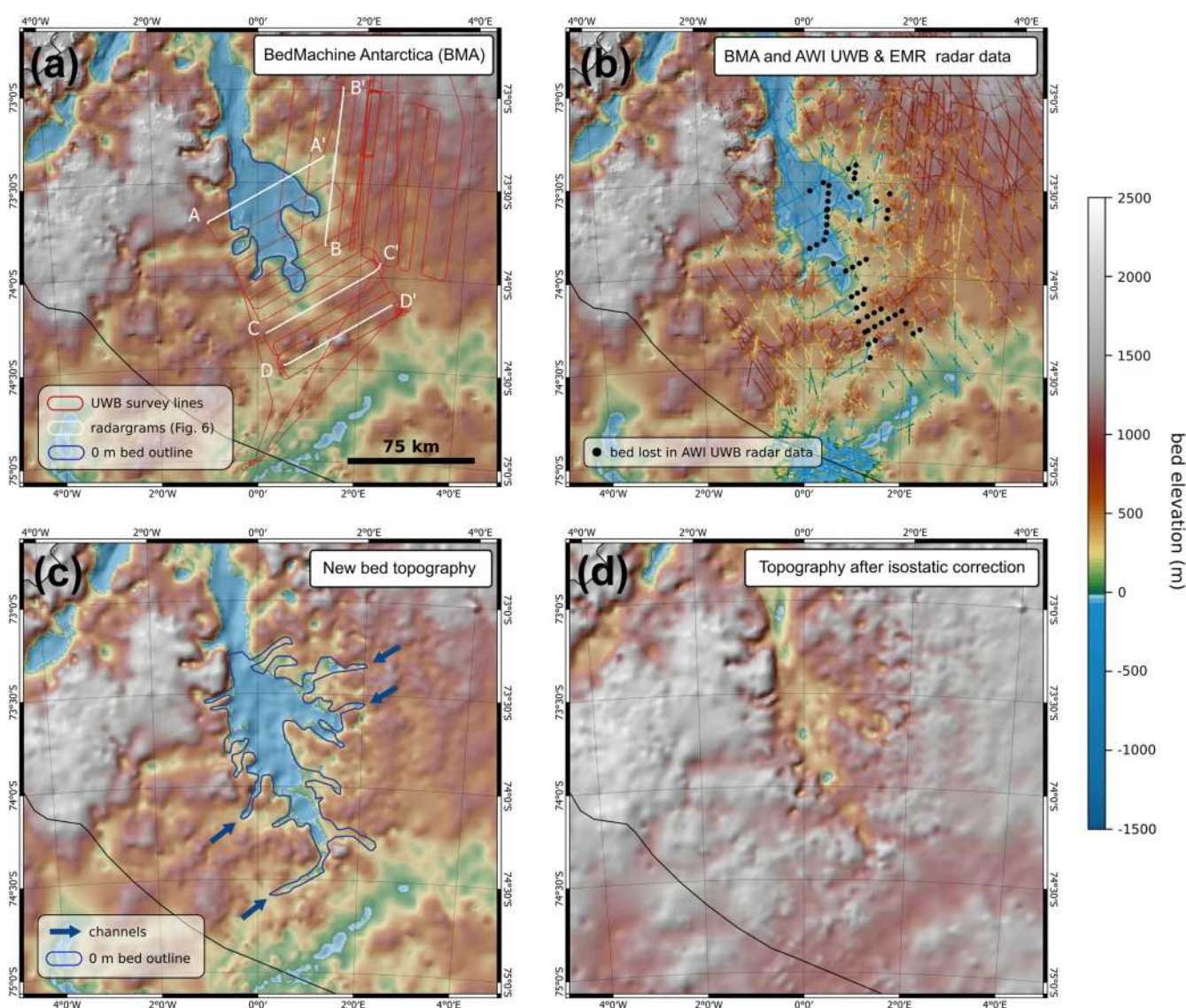


FIGURE 5 Bed topography in survey area. (a) BMA bed topography and location of JURAS-2018 survey lines (red lines) and selected radargrams of Figure 6 (white lines) with BMA in background. (b) The BMA topography is superimposed by AWI EMR and AWI UWB bed topography along the survey lines. Furthermore, significant bed reflection data gaps of the AWI UWB data are highlighted with black dots. (c) The new interpolated bed and an outline highlighting the extent of the valley network that lies below sea level. The outline was produced on the basis of the new bed topography DEM in combination with the topography data and gaps along the flight lines in part (b). (d) Bed topography after isostatic correction [Color figure can be viewed at wileyonlinelibrary.com]

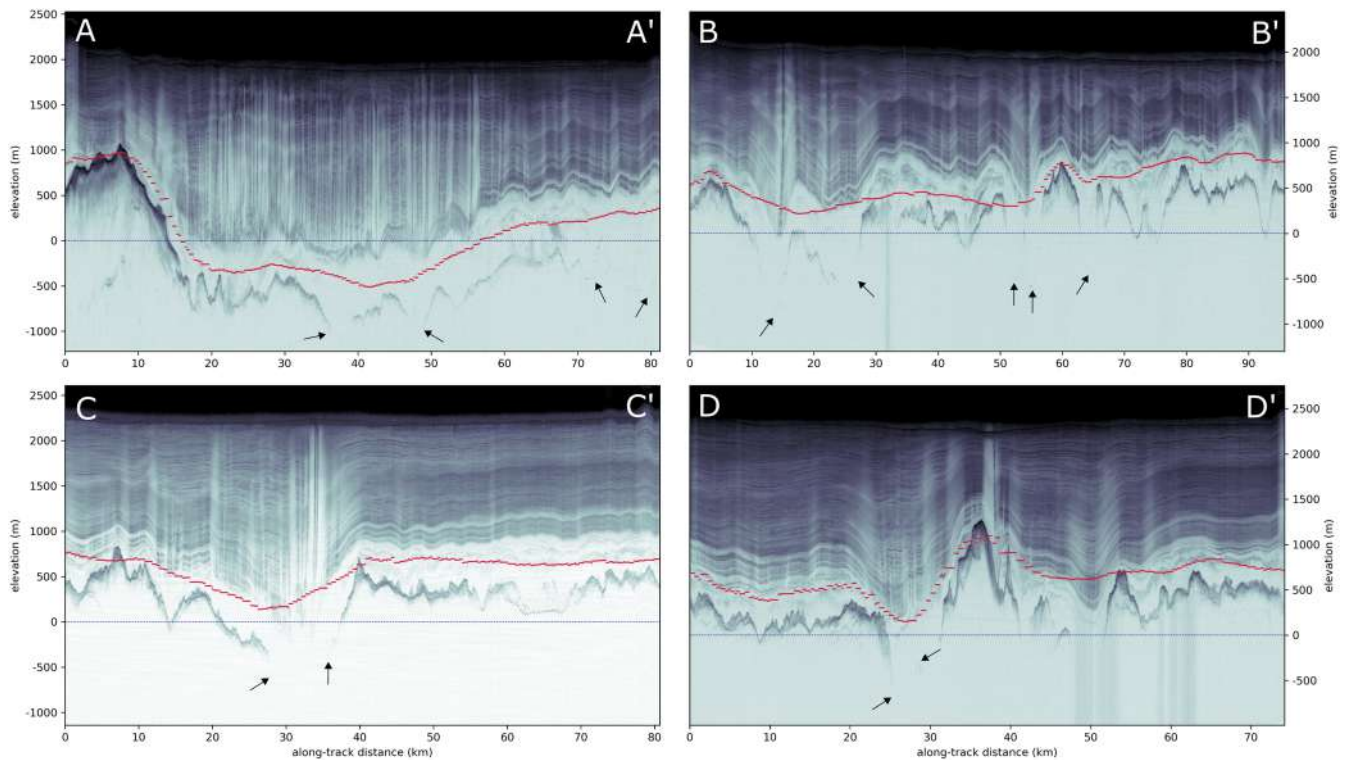


FIGURE 6 JURAS-2018 radargrams showing internal ice layering and bed topography in the onset region of JG. Profile locations are indicated in Figure 5a. The red dashed line represents the BMA bed topography elevation, while the blue line represents present sea level. Deep and faint bed reflections are indicated with black arrows [Color figure can be viewed at wileyonlinelibrary.com]

3. A network of very fine channels (~5 km width) runs perpendicular to the ice-flow direction (Figure 5c). These channels merge with the Jutulstraumen Graben. The network continues further southwards, where it connects to the adjacent inland basin.

3.2 | Valley morphology

The bed topography in the southern set of radar profiles shows generally different characteristic valley depths (D), valley ratios (R) and V -index than in the northern set of radar profiles (Figure 7a–c). Valleys located in the southern set are deeper (high D), wider (low R) and relatively more U-shaped (high and positive V -index) than their northern counterparts. Although data gaps prevented the calculation of statistics for crossings of the main JG valleys, it is clear from those reflections that are available that they, too, class as deep, wide, U-shaped valleys (see Figure 6a,c,d).

Based on the spatial distribution of the valley parameters, we define three regions with characteristic parameter combinations:

1. A region of wide and deep U-shaped valleys (black outline in Figure 7d). The main trunk of JG represents the largest valley structure in this region. This area shows the lowest bed elevation on average, up to several hundred metres below present sea level (see Figure 6a).
2. A region of wide and shallow U-shaped valleys (red outline in Figure 7d). A representative radargram for this region is shown in Figure 7 (V_2). This region shows a bed elevation range around 0–1000 m above sea level.

3. A region of shallow and narrow V- and U-shaped valleys (blue outline in Figure 7d). The radargram in Figure 7 (V_1) illustrates the characteristic valley geometries for this region. We also note that this area shows the highest overall bed topography, with elevations of around 500–2000 m.

The radargram in Figure 7 (V_3) shows a mix between the characteristics of the black and blue outlined regions in Figure 7d. Deeper sections of the bed topography are incised by deep U-shaped valleys. The central section with higher elevation shows smaller V- and U-shaped valley depths.

3.3 | Basal roughness

Figure 8 shows the three roughness parameters (the spectral vertical and horizontal roughnesses, ξ and η , as well as RMS height, χ) and their relationship to the topographic setting and ice surface flow velocity.

The highest vertical roughness values in the surveyed region tend to be concentrated below and around the main trunk of JG in a region that we refer to as *Zone a* (white dashed outline in Figure 8). *Zone a* hosts the largest valleys and the highest overall RMS height values, which peak well in excess of 400 m. The distribution of RMS height and spectral vertical roughness varies systematically with the distribution of deep and shallow valleys. *Zone a* also hosts all those data gaps in which the bed could not be detected, and in which higher vertical roughness values and longer wavelengths are expected.

Zone b (marked with a black dashed outline east of *Zone a*) shows a distinctive pattern of low vertical roughness and low RMS height.

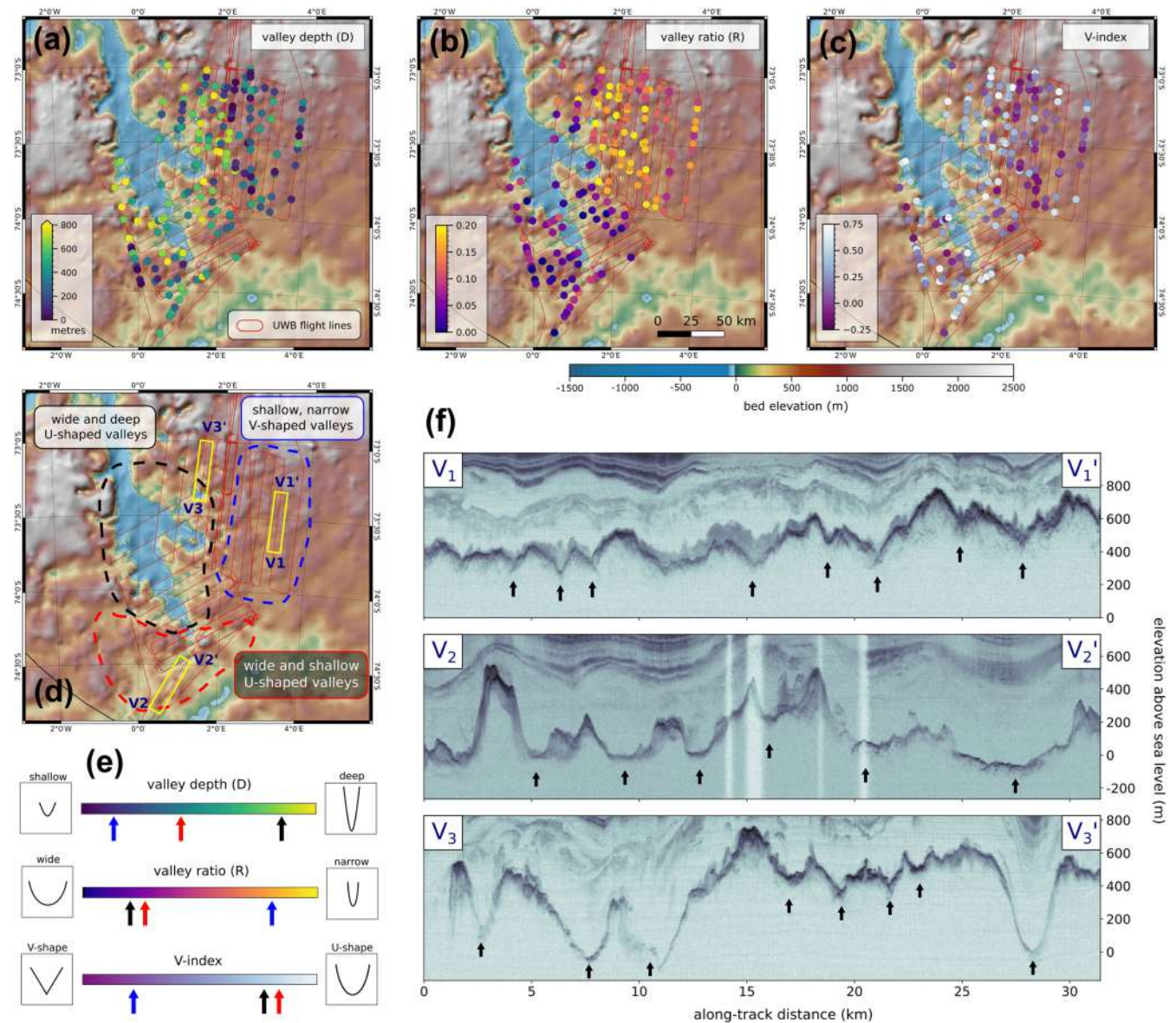


FIGURE 7 (a–c) Analysis of valley geometries (valley depth D , valley ratio R and V -index, respectively). In part (d) we define three regions characterised by contrasting valley statistics. The average characteristics for each region are indicated by the black, blue and red arrows in panel (e) and summarised by idealised sketches next to the colour bars. (f) Three radar profiles ($V_{1,2,3}$) showing the contrasting ice bed morphologies in the three regions. Radargram V_3 highlights the sudden change of valley geometries along a profile at the margin of JG. Black arrows mark valleys that we considered for our analysis (see Figure 4). Profile locations are indicated in part (d) inside yellow boxes [Color figure can be viewed at wileyonlinelibrary.com]

Here, the ice-flow velocity is slightly lower than in *Zone a*, while bed topography is more elevated than in the west. In contrast, the horizontal roughness is similar between *Zones a* and *b*. Shorter wavelengths are more dominant in the eastern part of the northern radar set than in the western part.

3.4 | Hypsometry

Analysis of the elevations reveals that, in addition to their contrasting basal roughnesses, *Zones a* and *b* are hypsometrically distinct (Figure 8d). In *Zone a*, bed elevation values scatter within a range of 1700 m, with a maximum at 1000–1400 m elevation. Hence the data are asymmetrically concentrated towards high elevations. This distribution does not include those low elevations that would have been encountered over gaps in the UWB data. The distribution of bed

elevations in *Zone b* is narrower and, on average, higher. Its shape is approximately normal, with a slightly higher concentration of counts on its low-elevation flank. Analysis of combined elevations from both zones shows a similar pattern overall to that in *Zone a*.

3.5 | Water flow routing

The water flow starting at high-elevation regions within the DML mountain chain is distributed towards three main catchment areas (Figure 8c):

1. Catchment C_A leads into the main topographic depression below what is now JG and covers the northeastern part of the present-day ice drainage basin. Most of the routing pathways of this catchment are located within *Zone a*.

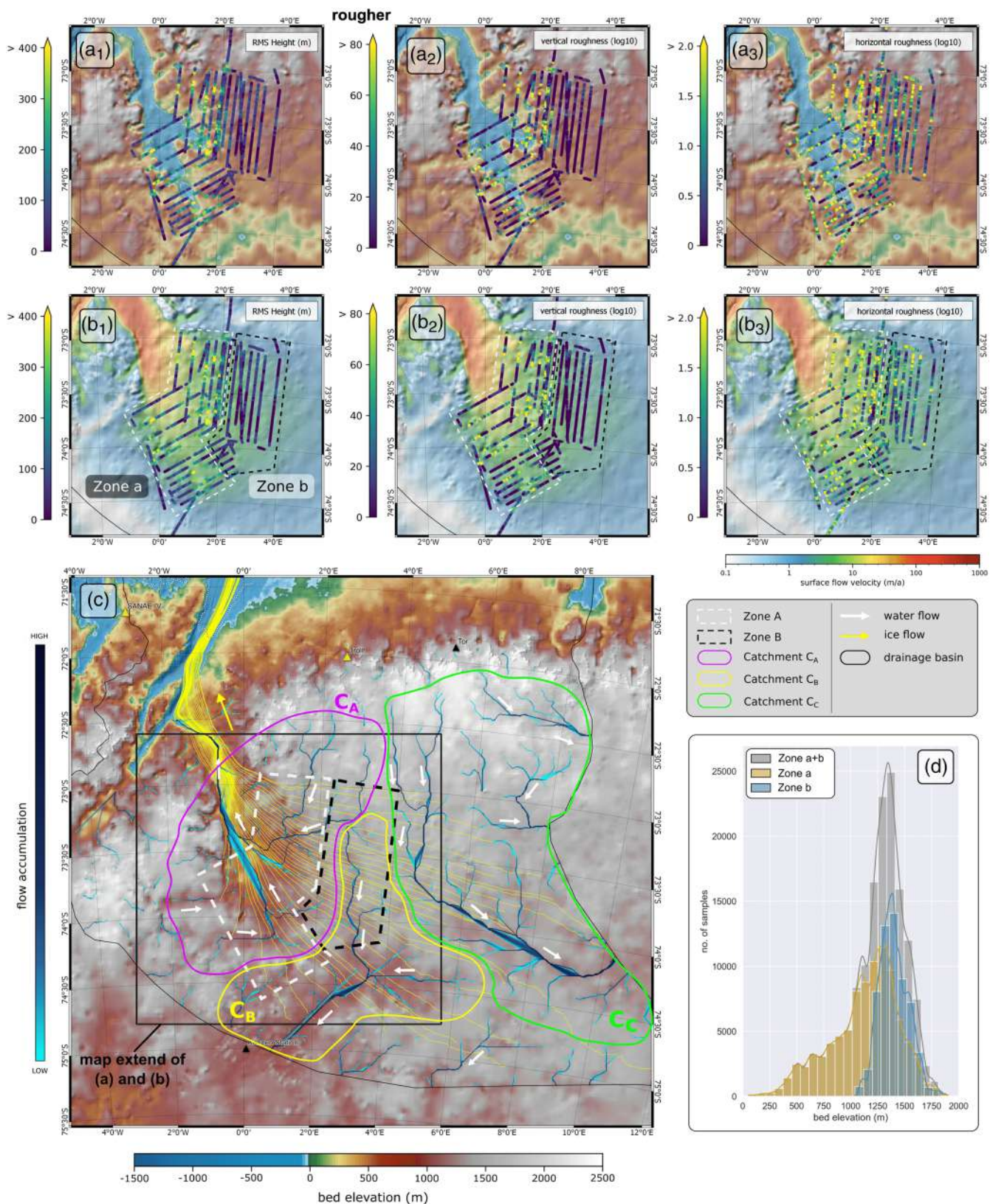


FIGURE 8 Results of basal roughness, water flow routing and hypsometric analyses. (a₁, 2, 3, b₁, 2, 3) Parameters for RMS height, spectral vertical roughness and horizontal roughness plotted over the BMA bed topography and ice-flow velocity, respectively. In panel (b) we divide the radar lines into two zones of distinctly differing basal roughness. (c) Water flow routing on the isostatically compensated bed elevation for a simulated ice-free region. The flow accumulation colour code represents the number of accumulated (upstream) cells. Yellow lines indicate the present ice-flow trajectories. The extent of the maps in panels (a) and (b) is indicated with a black outline. The general water flow direction is indicated by white arrows. We divide the water flow routing into three main catchments (C_{A,B,C}). The result of the hypsometric analyses of Zones a and b is presented in panel (d) [Color figure can be viewed at wileyonlinelibrary.com]

2. The second catchment, C_B , leads towards a topographic depression in the south of the present-day ice drainage basin. The topography leads most of the water into the neighbouring Slessor catchment (Mouginot & Rignot, 2017) to the west. Most of the radar survey lines of *Zone b* are located in this catchment. Furthermore, the EPICA ice core is located at the southwestern tip of this catchment.
3. Catchment C_C is located in the eastern part of the drainage basin where ice-flow velocity is lowest. The flow routing indicates a flow direction towards the neighbouring Vigrid basin (after Mouginot & Rignot, 2017) towards the east.

The water routing pathways of catchment C_A correspond approximately to the present-day ice-flow direction and propagation of subglacial water. The flow directions of C_B and C_C , however, lead towards regions of higher present-day ice thicknesses and therefore in the opposite direction to that of present ice flow. Thus the direction of water flow on the isostatically adjusted bed topography may in part correspond to the current subglacial hydrology (Livingstone et al., 2013), which is not parallel to the direction of present ice flow. However, the current ice configuration is going to generally drive subglacial water flow towards the northern continental margin.

4 | INTERPRETATION AND DISCUSSION

4.1 | Bed topography and valley morphology

Bed topography construction via simple interpolation techniques such as those used to generate Bedmap2 (Fretwell et al., 2013) relies on the spatial data density of ice thickness measurements alone. Hence the deep bed relief at the onset of the main trunk of JG, where the bed could not be detected with radar techniques, is biased to shallower values in Bedmap2. The advantages of the mass conservation and streamline diffusion approach of Morlighem et al. (2017) over ordinary gridding techniques tend to be only minor in areas of slow flow, like in the upstream part of the JG but stronger further downstream in the Jutulstraumen Graben (see supplementary fig. S42 in Morlighem et al. (2020), where the authors compare the Bedmap2 and BedMachine Antarctica v01 bed topography).

U-shaped valleys are distinctive features that suggest selective linear erosion on a local to regional scale, and are thus an indication for the presence of warm-based ice at the time of erosion (Sugden & John, 1976). The deepest topographic depressions in the JG drainage area are located where present-day ice-flow velocity and acceleration are highest (Mouginot et al., 2019). This suggests that the region (black outline in Figure 7d) has experienced erosion over a long period. The wide but shallow U-shaped valleys in the upstream region (red outline in Figure 7d) are located close to the ice divide, where the ice column is thickest and current ice-flow velocities are low. This indicates that these valleys were probably not eroded under the present ice-sheet configuration. The locations, shapes and sizes of these valleys suggest they most likely formed in regions of tectonic or lithologic weakness, or by the exploitation of valleys in a pre-existing fluvial network (e.g., Baroni et al., 2005; Jordan et al., 2013; Rose et al., 2015).

As an ice sheet grows to an intermediate size over a pre-existing fluvial landscape, selective linear erosion will deepen and widen existing river valleys (Sugden, 1968, 1978). Ongoing ice-sheet growth may lead to the development of a cold base, concomitant with a reduction of sliding and increase in ice-bed coupling (Jamieson et al., 2010). As a consequence, ice flow will be dominated by internal deformation and ice-flow velocity will reduce (Creyts et al., 2014). At the base of the ice sheet, the consequence of all this may be a change from an erosive alpine environment to a passive setting, in which the bed undergoes little further modification. This kind of evolution may have occurred rapidly over the upstream part of the northern radar dataset (blue outline in Figure 7d), which reflects the lowest degree of glacial erosion in its average high elevation and the dominance of shallow, V-shaped valleys.

The relative orientation of the radar line to the valley pathways is the largest source of uncertainty in the valley geometry analysis. Oblique crossings will make valleys appear artefactually too wide (a potential candidate could be the rightmost valley in Figure 7 (V_2)). Artefacts like this will affect the determinations of valley ratio (R) and V -index but not of valley depth (D). Therefore, narrow and V-shaped valleys could potentially be under-represented in Figure 7b,c. The potential discrepancy between valley pathway and optimum radar line orientation mainly depends on the ice-flow direction at the time of valley formation.

4.2 | Basal roughness

Eisen et al. (2020) analysed basal roughness parameters for AWI EMR radar data on a continental scale in Antarctica. They observed low vertical roughness in the region east of our northern survey grid. This is consistent with low vertical roughness in *Zone b* (Figure 8) and indicates that similar low vertical roughness values are to be expected further east. Eisen et al. (2020) showed that basal roughness in this region is, on average, anisotropic in respect to the orientation of the radar lines to the direction of ice flow. The interpretation of basal roughness is thus limited and restricted to profiles perpendicular to ice flow. Several studies highlight the importance of radar profile orientation in respect to the interpretation of basal roughness values (e.g., Cooper et al., 2019; Falcini et al., 2018; Gudlaugsson et al., 2013; Rippin et al., 2014). Because our radar profiles are mainly oriented transverse to contemporary ice flow, we expect the vertical roughness to be, on average, higher compared to a random survey layout (which would contain more profiles running along valley directions). Similar to Rose et al. (2015) and Falcini et al. (2018), we note that the interpretation of low vertical roughness regions as indicative of fast ice flow is not valid in this area. In our study area, ice flow is fastest at the locations close to deeply incised topographic depressions. The low vertical roughness in the slow-flowing *Zone b* potentially represents an area of preserved landforms (similar to the findings of Rippin et al. 2014), which might have been protected from extensive glacial erosion. The relatively high vertical and horizontal roughness values in the slow-flowing central upstream region of *Zone a* may represent a region of former, more extensive, glacial erosion under a more restricted ice sheet, as suggested by Rippin et al. (2014) and Ross et al. (2014) at the West Antarctic Ice Sheet.

Most importantly, the analysis of spectral vertical roughness and RMS height supports a certain aspect of the valley geometry analysis, increasing the robustness of their interpretation. It has to be noted that the focus of our roughness analysis and the choice of our MW is that we are able to discriminate the different landscapes. The spatial clusters of deep valleys correlate with high vertical roughness and RMS height, whereas the locations of shallow valleys correlate with low vertical roughness and RMS height. Furthermore, we observe that in *Zone b* the combination of narrow, V-shaped valleys is consistent with the dominance of short horizontal wavelengths. We are aware that both roughness values and valley geometries depend on the orientation of the radar profiles. However, since both analyses are based on the same radar profiles, we can assume that they experience the same effects due to the orientation of the profiles.

4.3 | Hypsometry

The main differences in the hypsometric curves for *Zone a* and *Zone b* (Figure 8d) are in the location of the peak and the absolute distributions of bed elevations. Jamieson et al. (2014) relate hypsometric patterns to the topographic classifications of Sugden and John (1976). Furthermore, Brocklehurst and Whipple (2004) analysed different ice-free mountain regimes and found a relationship between the degree of glaciation and their hypsometric curves. Their analysis shows that hypsometric curves with maxima near higher elevations are indicative of fully glaciated landscapes, whereas maxima at lower elevations tend to characterise curves for non-glaciated landscapes. The broad distribution of bed elevation values (0–2000 m elevation) and the maximum towards higher values between 1000 and 1500 m elevation (as we observe in *Zone a*) can be interpreted as a fully glaciated landscape (Brocklehurst and Whipple, 2004) formed under selective linear erosion (Jamieson et al., 2014). By contrast, the high mean bed elevation values in *Zone b* (1000–1800 m) with a maximum at slightly lower bed elevation (1400 m) most likely point to a mainly alpine setting that has been slightly modified by erosion. The relatively high mean elevations of both zones also suggest that the survey area has not been subject to areal scour or long-term denudation.

4.4 | Landscape classification

Using the isostatically corrected bed topography (Figure 5d) as an approximation of the pre-glacial surface, we note that the deepest and widest U-shaped valleys extend down to present sea level (Figure 5d). The Jutulstraumen Graben is of tectonic origin, dating back to the ice-free Jurassic, and so must have been subject to a long period of fluvial erosion after its formation (Näslund, 2001). This suggests that the bed in *Zone a* would have been subsequently modified by selective linear glacial erosion (Sugden & John, 1976). The deep and wide U-shaped subglacial valleys in *Zone a* are likely candidates for pre-glacial fluvial activity and subsequent selective erosion after the onset of glaciation (Sugden & John, 1976). Hence the U-shaped valleys of *Zone a* are likely to follow the pre-existing fluvial system. It is likely that, regardless of the regional evolution in

the extent and thickness of ice and the location of ice divides, some portion of the region's ice has always flowed through the Jutulstraumen Graben towards the northern continental margin. The initial formation of the graben itself and the subsequent long-term erosional activity could explain the deeply incised relief. The graben may have acted as an 'attractor' for higher ice dynamics, which then increased erosion rates.

The analysis of basal roughness and hypsometry for the area east of the main trunk of JG (*Zone b* in Figure 8) points towards a largely preserved fluvial landscape whose origin precedes extensive glaciation (Rippin et al., 2014; Rose et al., 2015). This is supported by the predominant appearance of shallow and narrow valleys at the glacier bed and the less variable and generally more elevated topography (and the resulting hypsometry). The mix of V- and U-shaped valleys suggests that the bed has been locally modified by glacial erosion at some point in the past. However, the high elevation topography likely resulted in slower flow and cold-based conditions (Sugden & John, 1976) for a large part of its history, resulting in a limited degree of landscape modification. Erosion under cold-based ice is several orders of magnitude slower than under temperate ice (Stroeven et al., 2002; Thomson et al., 2010).

Jacobs et al. (1995) suggest that intensive denudation by weathering and fluvial erosion were important landforming processes in western DML during the uplift that followed continental break-up in the middle and late Mesozoic. The fluvial landscape preserved east of JG may have developed since then. The water-flow regime calculated for that landscape, in catchments C_B and C_C , does not correlate with that of the drainage basin of the modern-day JG (Figure 8d). Today, the mountains of DML prevent the ice from flowing directly towards the margin, while the thicker inland ice in the interior of the AIS prevents southward flow.

The present ice-sheet configuration likely causes only selective linear erosion in the deep valleys (Ross et al., 2012) connected to the Jutulstraumen Graben, where basal temperatures are probably above the pressure melting point (Pattyn, 2010). Elevated basal ice temperatures increase englacial attenuation, consistent with the fact that the locations where we are unable to detect a bed reflection all lie in the deepest parts of the deepest depressions with fastest-flowing ice.

4.5 | Basal thermal regime

Geothermal heat flow (GHF) at the base of the Antarctic Ice Sheet is a parameter which is subject to substantial uncertainty because it is difficult to measure in situ. Consequently, geophysical models diverge greatly. Van Liefferinge et al. (2018) compare existing GHF datasets (An et al., 2015; Fox Maule et al., 2005; Martos et al., 2017; Shapiro & Ritzwoller, 2004) to predict the probable distribution of basal ice that has been frozen over the last 1.5 million years. Their modelled area includes the ice divides at the upstream part of the JG drainage basin. Based on the individual GHF datasets, their modelling reveals it to be likely that the ice base has reached the pressure melting point at least once over the last 1.5 million years. Moreover, it has been shown that measured GHF in eastern DML is locally much higher than predicted by geophysical methods (Talalay et al., 2020), consistent with evidence for temperate bed conditions from the recovery of refrozen

subglacial water at the EPICA-DML drill site (Weikusat et al., 2017; Wilhelms et al., 2014). Modelling results and borehole observations indicate that large parts of the JG drainage basin's ice bed are likely to be temperate. In combination with ice flow, this should lead to subglacial erosion. What remains open to question is exactly how temperate conditions affect processes at the glacier bed under slow flow velocities and near the ice divides. In view of the apparent preservation of fluvial landscapes in the basin, it can be suggested that erosion in such settings may be limited to subglacial fluvial action with relatively limited consequences for landscapes.

4.6 | Landscape erosion and preservation

The bed morphology of the JG drainage system shows patterns of three successive and/or separate stages of landscape modification (Figure 9). We regionally extend our interpretation of the structures

we have classified in our study and define the following interpretation for landscape erosion and preservation: (1) a preserved fluvial landscape shaped by fluvial erosion, minimal glacial erosion and preserved thereafter; (2) a preserved glacial landscape, which was more strongly modified by selective linear erosion at some time in the past compared to (1); and (3) an active glacial landscape, in which the erosion has been long-lived and is still ongoing.

The glacial landscape close to the valley system of and further upstream (black and red outlines in Figure 9) was probably formed by a regional ice-cap glacier system during a period when Antarctica was influenced by a warmer climate than present (Holmlund & Näslund, 1994; Young et al., 2011). A former ice divide may have separated the two regions during this period (yellow dashed line in Figure 9). At some point, as ice coverage increased (Holmlund & Näslund, 1994), erosion terminated in the U-shaped valleys in the south and west (red dashed arrows in Figure 9), but continued further north where ice surface velocities are still fast today (black dashed

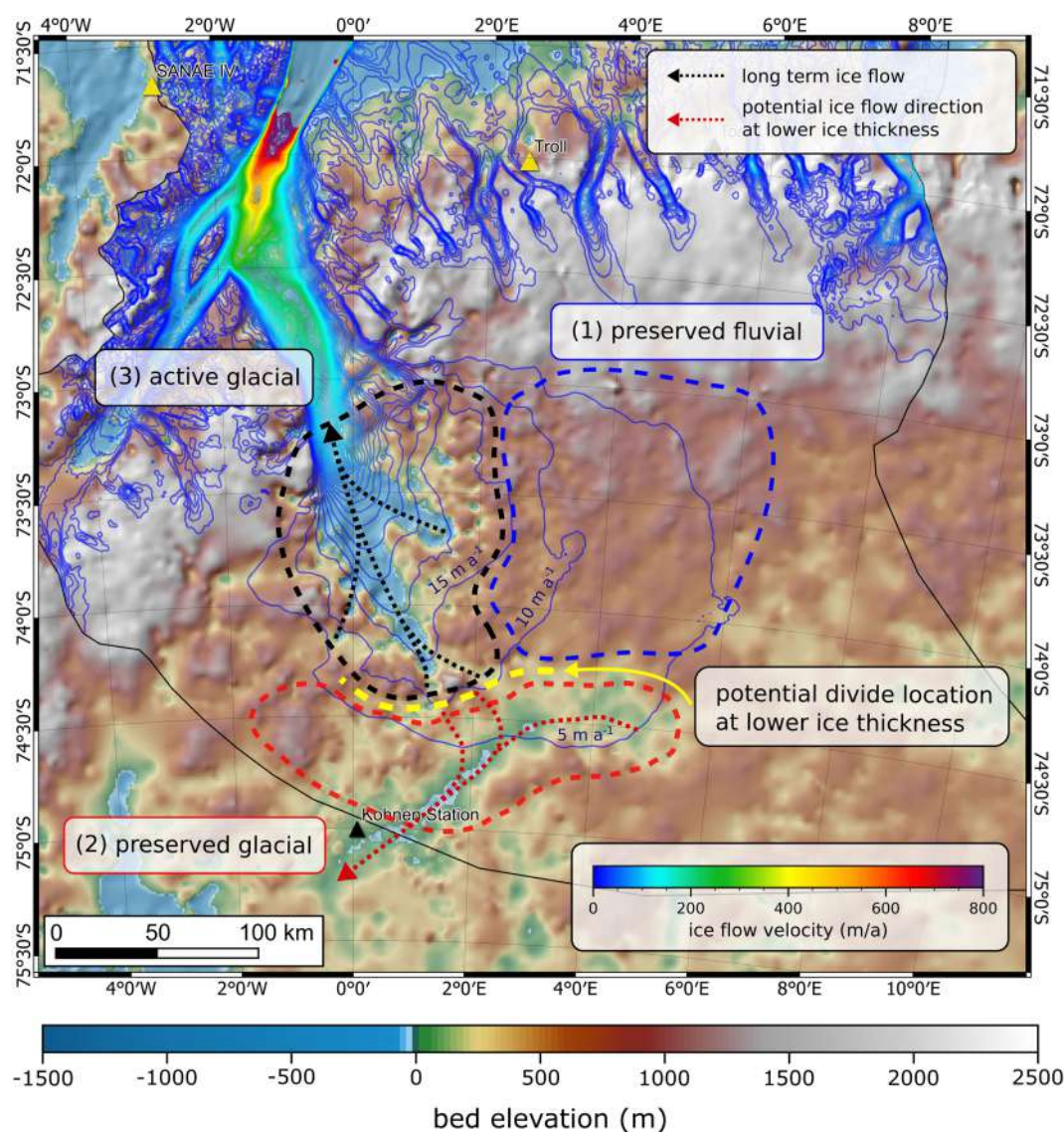


FIGURE 9 Summary of our landscape interpretation for the JG drainage system. The active glacial system (black dashed outline) is located in the immediate surroundings of the JG main trunk where the ice flow accelerates to join it. The preserved fluvial system (blue dashed outline) is located to the east and the preserved inactive glacial system (red dashed outline) to the west and south of the JG main trunk. The respective outlines do not represent physically fixed boundaries but instead areas of dominant landscape characteristics. Ice-flow velocity is indicated with contour lines in a 5 m a^{-1} interval. Hence the ice flow velocity of the large region south and east of the 5 m a^{-1} contour line is less than 5 m a^{-1} [Color figure can be viewed at wileyonlinelibrary.com]

arrows in Figure 9). The precondition of the initially large-scale graben likely created a positive feedback causing faster ice flow, more melt-water and, thus, enhanced erosion. In addition, at locations where the ice sheet grows beyond a critical size, we expect basal melting and the development of a subglacial water network (Creys et al., 2014). In our study area, this might explain the increased erosion rates that locally formed exceptionally deep valleys. Erosion mechanisms, such as plucking and abrasion, are mainly controlled by basal sliding, which requires in turn a lubricated bed (Hallet, 1996). By contrast, refreezing of subglacial water in cold-based areas with a thinner ice thickness (Creys et al., 2014) is probably also a factor in the preservation of the fluvial landscape in the east.

Jamieson et al. (2010) use an ice-sheet and erosion model to investigate the subglacial landscape evolution of Antarctica since the Oligocene (34 million years ago). These authors use three different stages for their simulations (see Table 1 in Jamieson et al., 2010) where: (a) ice sheets grow and shrink at similar spatial scales to northern hemisphere Pleistocene ice sheets (34–14 million years before present); (b) cooling shifts the system towards development of a continental polar ice sheet (14–13.6 million years ago); and (c) the continental polar ice sheet stabilises and subsequently experiences only minor changes (13.6 million years ago to present). In order to establish a rough timing for the landscape evolution in the JG drainage system, we compare the erosion rates modelled by Jamieson et al. (2010) with our landscape classification. For the comparison we mainly rely on the results shown in fig. 6 in Jamieson et al. (2010).

The model predicts that high erosion rates at the Jutulstraumen Graben developed at the end of stage (a) and persisted there ever since. We note that, at the beginning of stage (a), high erosion rates were restricted to the high-elevation areas of the DML mountains. The fluctuating regional ice caps may not have seen the development of a stable ice divide around the JG drainage basin like today's. Instead, they may have drained via ice streams running both northwards through the Jutulstraumen Graben and towards the southwest. We find that modelled erosion rates in the lower-elevation regions (e.g., in the Jutulstraumen Graben and further upstream) must have been higher than in the highlands. This is consistent with evidence for reduced erosion in *Zone b*. We note that the erosion rates in our survey region during stages (b) and (c) correspond to those of today's ice-dynamic setting. That is, constant high erosion rates are to be found only in the Jutulstraumen Graben.

Considering the modelling of Jamieson et al. (2010), we can estimate that the bed in *Zone b* was most likely modified in the early stages of glaciation of Antarctica (34–14 million years ago) during ice coverage minima when erosion was most intense at high altitudes. By contrast, we consider the U-shaped valleys upstream of the main trunk of JG were formed during a cycle of greater ice extent in stage (a), while more and faster ice was streaming towards the southwest. Erosion in both these settings probably ceased with the onset of continental-scale glaciation of Antarctica in stage (b) 14–13.6 million years ago. Hence we conclude that the modelling results of Jamieson et al. (2010) are a plausible explanation for the morphological structures identified in our study. The improvement of landscape development models, such as the modelling of Jamieson et al. (2010), are important for the understanding of the past behaviour of the AIS but require robust paleo-topographic reconstructions (Paxman et al., 2020).

5 | SUMMARY AND CONCLUSIONS

The landscape of Antarctica has been evolving for tens of millions to 100 million years. Since the colder climate in Antarctica around 14 million years ago fluvial erosion only played a minor role in the landscape modification (Sugden & Jamieson, 2018). The thick ice cover has protected the underlying landscape where the ice is stagnant and cold based. In our work, we demonstrated that previous fluvial and glacial activity can be preserved beneath thick ice masses in western DML, also highlighting the longevity of the local dynamic setting of ice flow. Their geomorphological characteristics reflect the processes and ice-dynamic setting under which they were created (Jamieson et al., 2014; Sugden & Jamieson, 2018), which can serve as constraints for modelling past ice dynamics (Rippin et al., 2014).

We extend the radar data inventory for central DML, and in particular for the immediate surroundings of the JG onset region to characterise the modification stages of the subglacial landscape. We use the existing bed topography data in combination with new high-resolution UWB radar data to analyse the morphology of the bed in the JG drainage system. For our analysis, we rely on the distribution of bed elevations (hypsoetry), parametrisations of the roughness of the bed, estimates of subglacial valley types, and analyses of their slopes and connectivity for characterisation of a pre-glacial fluvial system.

The glacial landscape in the JG drainage system can be divided into three different regimes:

1. The area of contemporary high ice-flow velocities marking JG, which represents an alpine landscape that has been extensively modified by selective linear (glacial) erosion. The deep U-shaped valleys in this area were probably initiated by fluvial erosion and subsequently modified by long-term glacial erosion.
2. The area upstream of JG in the south and west of the drainage system, where fluvial valleys were modified by a short period of glacial erosion before ice drainage in them ceased. The resulting U-shaped valleys are relatively small in comparison to the large valleys in the vicinity of the main trunk of JG. This area is close to the present-day ice divide, and ice-flow velocities are consequently low ($<5 \text{ m a}^{-1}$).
3. The high-elevation region east of JG, where the ice is slowly flowing under the present ice-sheet configuration. The abundance of small-scale V- and U-shaped valleys indicates the activity of an ancient alpine fluvial network which has been only locally and slightly modified by glacial erosion.

The transformation to the current ice-sheet configuration around 14 million years ago has limited basal erosion everywhere except in the direct vicinity of JG, where long-term ice-stream activity has excavated several kilometres deep subglacial valleys. This applies in particular to the cold-based high-elevation area in the east, where the ice sheet is trapped between the DML mountains in the north and the much thicker ice further south, resulting in the preservation of the pre-glacial fluvial landscape at the ice-sheet base. The Jutulstraumen Graben is presently the only passage for ice to flow towards the ice-sheet margin. The ice-dynamic setting must have been different to the present one to create the U-shaped valleys, which reach up almost to the ice divide in the southwest of the survey area. The high

probability that the ice base of our survey region is at pressure melting point suggests a higher potential for erosion than if frozen to the bed. However, erosion in this area is limited as long as ice-flow velocities are low. The landscape evolution established in this study is in good agreement with modelled erosion rates in Antarctica over the last 34 million years by Jamieson et al. (2010).

ACKNOWLEDGEMENTS

We thank the Kenn Borek crew as well as Martin Gehrman and Sebastian Spelz of AWI's technical staff of the research aircraft *Polar 6*. John Paden (University of Kansas) assisted remotely during the field campaign. We would like to thank Tobias Binder for the implementation of the AWI UWB radar as well as an acquisition backup system. Without his work, it would not have been possible to realise the campaign. Logistical support in Antarctica was provided at Troll Station (Norway), Novolazarevskaja-Station (Russia) and Kohnen Station (Germany). We acknowledge the use of the CReSIS toolbox from CReSIS generated with support from the University of Kansas, NASA Operation IceBridge grant NNX16AH54G, and NSF grants ACI-1443054, OPP-1739003 and IIS-1838230. The authors would like to thank Emerson E&P Software, Emerson Automation Solutions, for providing licences in the scope of the Emerson Academic Program. Furthermore, we acknowledge support by the Open Access Publication Funds of Alfred-Wegener-Institut Helmholtz-Zentrum für Polar- und Meeresforschung. Steven Franke was funded by the AWI Strategy fund and Daniela Jansen by the AWI Strategy fund and the Helmholtz Young investigator group HGF YIG VH-NG-802.

CONFLICT OF INTEREST

The authors declare no conflict of interest.










AUTHOR CONTRIBUTIONS

Steven Franke, Hannes Eisermann, Daniela Jansen and Wilfried Jokat designed the study with contributions of Heinz Miller and Olaf Eisen. Steven Franke and Hannes Eisermann wrote the manuscript. Daniela Jansen designed the JURAS-2018 radar survey and acquired the data together with Steven Franke. Steven Franke performed the data processing and generated the results with contributions from Daniela Jansen, Veit Helm and Daniel Steinhage and Jönlund Asseng. All authors discussed and commented the manuscript.

DATA AVAILABILITY STATEMENT

Ice thickness data from the complete JURAS-2018 AWI UWB radar survey (Franke et al., 2020) are available at <https://doi.pangaea.de/10.1594/PANGAEA.911475>. Ice surface velocities from Mougnot et al. (2019) are available at the National Snow and Ice Data Center (NSIDC), <https://doi.org/10.7280/D10D4Z>. The drainage system boundaries (Mougnot & Rignot, 2017) can be obtained here: <https://doi.org/10.5067/AXE4121732AD>. The Landsat Image Mosaic of Antarctica (LIMA; Bindschadler et al. (2008)) can be downloaded at <https://lima.usgs.gov>. The BedMachine Antarctica V01 dataset from Morlighem et al. (2019) is available at <https://nsidc.org/data/nsidc-0756>. The locations of Antarctic research facilities were obtained from the Quantarctica3 package (Matsuoka et al., 2021; <https://www.npolar.no/quantarctica/>).

ORCID

Steven Franke  <https://orcid.org/0000-0001-8462-4379>
 Hannes Eisermann  <https://orcid.org/0000-0002-5604-6484>
 Wilfried Jokat  <https://orcid.org/0000-0002-7793-5854>
 Graeme Eagles  <https://orcid.org/0000-0001-5325-0810>
 Heinrich Miller  <https://orcid.org/0000-0003-1015-2828>
 Daniel Steinhage  <https://orcid.org/0000-0003-4737-9751>
 Veit Helm  <https://orcid.org/0000-0001-7788-9328>
 Olaf Eisen  <https://orcid.org/0000-0002-6380-962X>
 Daniela Jansen  <https://orcid.org/0000-0002-4412-5820>

REFERENCES

- Airy, G.B. (1855) III. On the computation of the effect of the attraction of mountain-masses, as disturbing the apparent astronomical latitude of stations in geodetic surveys. *Philosophical Transactions of the Royal Society of London*, 145, 101–104. <https://royalsocietypublishing.org/doi/abs/10.1098/rstl.1855.0003>
- An, M., Wiens, D.A., Zhao, Y., Feng, M., Nyblade, A., Kanao, M. et al. (2015) Temperature, lithosphere–asthenosphere boundary, and heat flux beneath the Antarctic Plate inferred from seismic velocities. *Journal of Geophysical Research: Solid Earth*, 120(12), 8720–8742. <https://agupubs.onlinelibrary.wiley.com/doi/abs/10.1002/2015JB011917>
- Baroni, C., Noti, V., Ciccacci, S., Righini, G. & Salvatore, M.C. (2005) Fluvial origin of the valley system in northern Victoria Land (Antarctica) from quantitative geomorphic analysis. *Bulletin of the Geological Society of America*, 117(1–2), 212–228. <https://doi.org/10.1130/B25529.1>
- Bindschadler, R., Vornberger, P., Fleming, A., Fox, A., Mullins, J., Binnie, D. et al. (2008) The Landsat Image Mosaic of Antarctica. *Remote Sensing of Environment*, 112(12), 4214–4226. <http://www.sciencedirect.com/science/article/pii/S003442570800223X>
- Brocklehurst, S.H. & Whipple, K.X. (2004) Hypsometry of glaciated landscapes. *Earth Surface Processes and Landforms*, 29(7), 907–926. <https://doi.org/10.1002/esp.1083>
- Brozović, N., Burbank, D.W. & Meigs, A.J. (1997) Climatic limits on landscape development in the northwestern Himalaya. *Science*, 276(5312), 571–574. <https://doi.org/10.1126/science.276.5312.571>
- Callens, D., Matsuoka, K., Steinhage, D., Smith, B., Witrant, E. & Pattyn, F. (2014) Transition of flow regime along a marine-terminating outlet glacier in East Antarctica. *The Cryosphere*, 8(3), 867–875. <https://doi.org/10.5194/tc-8-867-2014>
- Conrad, O., Bechtel, B., Bock, M., Dietrich, H., Fischer, E., Gerlitz, L. et al. (2015) System for Automated Geoscientific Analyses (SAGA) v. 2.1.4. *Geoscientific Model Development*, 8(7), 1991–2007. <https://gmd.copernicus.org/articles/8/1991/2015/>
- Cooper, M.A., Jordan, T.M., Schroeder, D.M., Siegert, M. J., Williams, C. N. & Bamber, J.L. (2019) Subglacial roughness of the Greenland Ice Sheet: Relationship with contemporary ice velocity and geology. *The Cryosphere*, 13(11), 3093–3115. <https://tc.copernicus.org/articles/13/3093/2019/>
- CReSIS. (2020) CReSIS Toolbox [computer software], Lawrence, Kansas, USA. Available at: <https://github.com/CReSIS>, https://ops.cresis.ku.edu/wiki/index.php/Main_Page
- Creyts, T.T., Ferraccioli, F., Bell, R.E., Wolovick, M., Corr, H., Rose, K. C. et al. (2014) Freezing of ridges and water networks preserves the Gamburtsev Subglacial Mountains for millions of years. *Geophysical Research Letters*, 41(22), 8114–8122. <https://agupubs.onlinelibrary.wiley.com/doi/abs/10.1002/2014GL061491>
- Cui, X., Jeofry, H., Greenbaum, J.S., Guo, J., Li, L., Lindzey, L.E. et al. (2020) Bed topography of Princess Elizabeth Land in East Antarctica. *Earth System Science Data*, 12(4), 2765–2774. <https://essd.copernicus.org/articles/12/2765/2020/>
- Eagles, G., Karlsson, N.B., Ruppel, A., Steinhage, D., Jokat, W. & Läufer, A. (2018) Erosion at extended continental margins: Insights from new

- aerogeophysical data in eastern Dronning Maud Land. *Gondwana Research*, 63, 105–116. <https://www.sciencedirect.com/science/article/abs/pii/S1342937X18301655>
- Eisen, O., Winter, A., Steinhage, D., Kleiner, T. & Humbert, A. (2020) Basal roughness of the East Antarctic Ice Sheet in relation to flow speed and basal thermal state. *Annals of Glaciology*, 61(81), 162–175. <https://doi.org/10.1017/aog.2020.47>
- Eisermann, H., Eagles, G., Ruppel, A., Smith, E. & Jokat, W. (2020) Bathymetry beneath ice shelves of western Dronning Maud Land, East Antarctica, and implications on ice shelf stability. *Geophysical Research Letters*, 47(12), e2019GL086724. <https://doi.org/10.1029/2019GL086724>
- Elliot, D.H. (1992) Jurassic magmatism and tectonism associated with Gondwanaland break-up: An Antarctic perspective. *Geological Society, London, Special Publications*, 68(1), 165–184. <https://doi.org/10.1144/GSL.SP.1992.068.01.11>
- Falcini, F.A.M., Rippin, D.M., Krabbendam, M. & Sselby, K.A. (2018) Quantifying bed roughness beneath contemporary and palaeo-ice streams. *Journal of Glaciology*, 64(247), 822–834. <https://doi.org/10.1017/jog.2018.71>
- Ferraccioli, F., Jones, P.C., Curtis, M.L. & Leat, P.T. (2005) Subglacial imprints of early Gondwana break-up as identified from high resolution aerogeophysical data over western Dronning Maud Land, East Antarctica. *Terra Nova*, 17(6), 573–579. <https://doi.org/10.1111/j.1365-3121.2005.00651.x>
- Fox Maule, C., Purucker, M.E., Olsen, N. & Mosegaard, K. (2005) Heat flux anomalies in Antarctica revealed by satellite magnetic data. *Science*, 309(5733), 464–467. <https://science.sciencemag.org/content/309/5733/464>
- Franke, S., Jansen, D., Beyer, S., Neckel, N., Binder, T., Paden, J. & Eisen, O. (2021) Complex basal conditions and their influence on ice flow at the onset of the Northeast Greenland Ice Stream. *Journal of Geophysical Research: Earth Surface*, 126(3), e2020JF005689. <https://doi.org/10.1029/2020JF005689>
- Franke, S., Jansen, D., Binder, T., Dörr, N., Helm, V., Paden, J. et al. (2020) Bed topography and subglacial landforms in the onset region of the Northeast Greenland Ice Stream. *Annals of Glaciology*, 61(81), 143–153. <https://doi.org/10.1017/aog.2020.12>
- Franke, S., Jansen, D. & Helm, V. (2020) Ice thickness from Jutulstraumen Glacier recorded with the airborne AWI UWB radar system, Antarctica. <https://doi.pangaea.de/10.1594/PANGAEA.911475>
- Fretwell, P., Pritchard, H.D., Vaughan, D.G., Bamber, J.L., Barrand, N.E., Bell, R. et al. (2013) Bedmap2: Improved ice bed, surface and thickness datasets for Antarctica. *The Cryosphere*, 7(1), 375–393. <https://www.the-cryosphere.net/7/375/2013/>
- Goeller, S., Steinhage, D., Thoma, M. & Grosfeld, K. (2016) Assessing the subglacial lake coverage of Antarctica. *Annals of Glaciology*, 57(72), 109–117. <https://doi.org/10.1017/aog.2016.23>
- Gray, D.R., Foster, D.A., Meert, J.G., Goscombe, B.D., Armstrong, R., Trouw, R.A.J. & Passchier C.W. (2008) A damara orogen perspective on the assembly of southwestern Gondwana. *Geological Society, London, Special Publications*, 294(1), 257–278. <https://doi.org/10.1144/SP294.14>
- Gudlaugsson, E., Humbert, A., Winsborrow, M. & Andreassen, K. (2013) Subglacial roughness of the former Barents Sea Ice Sheet. *Journal of Geophysical Research: Earth Surface*, 118(4), 2546–2556. <https://agupubs.onlinelibrary.wiley.com/doi/abs/10.1002/2013JF002714>
- Hale, R., Miller, H., Gogineni, S., Yan, J. B., Leuschen, C., Paden, J. & Li, J. (2016) Multi-channel ultra-wideband radar sounder and imager. In: 2016 IEEE International Geoscience and Remote Sensing Symposium (IGARSS), 10–15 July 2016. IEEE: Beijing, China, pp. 2112–2115.
- Hallet, B. (1996) Glacial quarrying: A simple theoretical model. *Annals of Glaciology*, 22, 1–8. <https://doi.org/10.3189/1996AoG22-1-1-8>
- Hirano, M. & Aniya, M. (1988) A rational explanation of cross-profile morphology for glacial valleys and of glacial valley development. *Earth Surface Processes and Landforms*, 13(8), 707–716. <https://onlinelibrary.wiley.com/doi/abs/10.1002/esp.3290130805>
- Holbourn, A., Kuhnt, W., Schulz, M. & Erlenkeuser, H. (2005) Impacts of orbital forcing and atmospheric carbon dioxide on Miocene ice-sheet expansion. *Nature*, 438(7067), 483–487. <https://www.nature.com/articles/nature04123>
- Holmlund, P. & Näslund, J.-O. (1994) Antarctica, formed by wet-based mountain glaciation and not by the present ice sheet. *Boreas*, 23, 139–148. <https://doi.org/10.1111/j.1502-3885.1994.tb00594.x>
- Holschuh, N., Christianson, K., Paden, J., Alley, R.B. & Anandkrishnan, S. (2020) Linking postglacial landscapes to glacier dynamics using swath radar at Thwaites Glacier Antarctica. *Geology*, 48(3), 268–272. <https://doi.org/10.1130/g46772.1>
- Howat, I.M., Porter, C., Smith, B.E., Noh, M.-J. & Morin, P. (2019) The Reference Elevation Model of Antarctica. *The Cryosphere*, 13(2), 665–674. <https://www.the-cryosphere.net/13/665/2019/>
- Høydal, O.A. (1996) A force-balance study of ice flow and basal conditions of Jutulstraumen, Antarctica. *Journal of Glaciology*, 42(142), 413–425. <https://doi.org/10.3189/S0022143000003403>
- Huybrechts, P., Steinhage, D., Wilhelms, F. & Bamber, J. (2000) Balance velocities and measured properties of the Antarctic ice sheet from a new compilation of gridded data for modelling. *Annals of Glaciology*, 30(1996), 52–60. <https://doi.org/10.3189/172756400781820778>
- Jacobs, J. (1991) Strukturelle Entwicklung und Abkühlungsgeschichte der Heimefrontfjella (Westliches Dronning Maud Land/Antarktika); Structural evolution and cooling history of the Heimefrontfjella (western Dronning Maud Land/Antarctica). *Berichte zur Polarforschung (Reports on Polar Research)*, 97, 1–141. https://doi.org/10.2312/BzP_0097_1991
- Jacobs, J., Ahrendt, H., Kreutzer, H. & Weber, K. (1995) K-Ar. ⁴⁰Ar-¹⁹Ar and apatite fission-track evidence for Neoproterozoic and Mesozoic basement rejuvenation event in the Heimefrontfjella and Mannefallknausane (East Antarctica). *Precambrian Research*, 75, 251–262. <https://www.sciencedirect.com/science/article/abs/pii/S0301926895800097>
- Jacobs, J., Fanning, C.M., Henjes-Kunst, F., Olesch, M. & Paech, H.-J. (1998) Continuation of the Mozambique Belt into East Antarctica: Grenville-age metamorphism and polyphase Pan-African high-grade events in central Dronning Maud Land. *Journal of Geology*, 106(4), 385–406. <https://doi.org/10.1086/516031>
- Jacobs, J., Hejl, E., Wagner, G.A. & Weber, K. (1992) Apatite fission track evidence for contrasting thermal and uplift histories of metamorphic basement blocks in western Dronning Maud Land. In *Recent Progress in Antarctic Earth Science*. Tokyo: Terrapub, pp. 323–330.
- Jacobs, J., Opås, B., Elburg, M.A., Läuffer, A., Estrada, S., Ksienzyk, A.K. et al. (2017) Cryptic sub-ice geology revealed by a U-Pb zircon study of glacial till in Dronning Maud Land, East Antarctica. *Precambrian Research*, 294, 1–14. <https://www.sciencedirect.com/science/article/abs/pii/S0301926817300591>
- Jacobs, J. & Thomas, R.J. (2004) Himalayan-type indenter-escape tectonics model for the southern part of the late Neoproterozoic–early Paleozoic East African–Antarctic orogen. *Geology*, 32(8), 721–724. <https://doi.org/10.1130/G20516.1>
- Jamieson, S.S.R., Stokes, C.R., Ross, N., Rippin, D.M., Bingham, R.G., Wilson, D.S. et al. (2014) The glacial geomorphology of the Antarctic ice sheet bed. *Antarctic Science*, 26(6), 724–741. <https://doi.org/10.1017/S0954102014000212>
- Jamieson, S.S.R., Sugden, D.E. & Hulton, N.R.J. (2010) The evolution of the subglacial landscape of Antarctica. *Earth and Planetary Science Letters*, 293(1–2), 1–27. <https://doi.org/10.1016/j.epsl.2010.02.012>
- Jokat, W., Boebel, T., König, M. & Meyer, U. (2003) Timing and geometry of early Gondwana breakup. *Journal of Geophysical Research: Solid Earth*, 108(B9), 2428. <https://doi.org/10.1029/2002JB001802>
- Jordan, T.A., Ferraccioli, F., Ross, N., Corr, H.F.J., Leat, P.T., Bingham, R.G. et al. (2013) Inland extent of the Weddell Sea Rift imaged by new aerogeophysical data. *Tectonophysics*, 585, 137–160. <http://www.sciencedirect.com/science/article/pii/S0040195112005689>
- King, E.C., Hindmarsh, R.C.A. & Stokes, C.R. (2009) Formation of megascale glacial lineations observed beneath a West Antarctic ice stream. *Nature Geoscience*, 2(8), 585–588. <https://doi.org/10.1038/ngeo581>
- Leinweber, V.T. & Jokat, W. (2012) The Jurassic history of the Africa–Antarctica corridor: New constraints from magnetic data on the conjugate continental margins. *Tectonophysics*, 530, 87–101. <https://www.sciencedirect.com/science/article/pii/S0040195111004641>

- Li, X., Sun, B., Siegert, M.J., Bingham, R.G., Tang, X., Zhang, D. et al. (2010) Characterization of subglacial landscapes by a two-parameter roughness index. *Journal of Glaciology*, 56(199), 831–836. <https://doi.org/10.3189/002214310794457326>
- Livingstone, S.J., Clark, C.D., Woodward, J. & Kingslake, J. (2013) Potential subglacial lake locations and meltwater drainage pathways beneath the Antarctic and Greenland ice sheets. *The Cryosphere*, 7(6), 1721–1740. <https://doi.org/10.5194/tc-7-1721-2013>
- Martos, Y.M., Catalán, M., Jordan, T.A., Golynsky, A., Golynsky, D., Eagles, G. & Vaughan D.G. (2017) Heat flux distribution of Antarctica unveiled. *Geophysical Research Letters*, 44(22), 11417–11426. <https://agupubs.onlinelibrary.wiley.com/doi/abs/10.1002/2017GL075609>
- Matsuoka, K., Skoglund, A., Roth, G., de Pomereu, J., Griffiths, H., Headland, R. et al. (2021) Quantarctica, an integrated mapping environment for Antarctica, the Southern Ocean, and sub-Antarctic islands. *Environmental Modelling and Software*, 140, 105015. <https://www.sciencedirect.com/science/article/pii/S136481522100058X>
- Mieth, M. & Jokat, W. (2014) New aeromagnetic view of the geological fabric of Southern Dronning Maud Land and Coats Land, East Antarctica. *Gondwana Research*, 25(1), 358–367. <http://www.sciencedirect.com/science/article/pii/S1342937X13001226>
- Morlighem, M., Rignot, E., Binder, T., Blankenship, D., Drews, R., Eagles, G. et al. (2020) Deep glacial troughs and stabilizing ridges unveiled beneath the margins of the Antarctic ice sheet. *Nature Geoscience*, 13(2), 132–137. <https://doi.org/10.1038/s41561-019-0510-8>
- Morlighem, M., Rignot, E., Binder, T., Blankenship, D., Drews, R., Eagles, G. et al. (2019) Deep glacial troughs and stabilizing ridges unveiled beneath the margins of the Antarctic ice sheet. *Nature Geoscience*, 13(2), 132–137. <http://www.nature.com/articles/s41561-019-0510-8>
- Morlighem, M., Williams, C.N., Rignot, E., An, L., Arndt, J.E., Bamber, J.L. et al. (2017) BedMachine v3: Complete bed topography and ocean bathymetry mapping of Greenland from multibeam echo sounding combined with mass conservation. *Geophysical Research Letters*, 44(21), 11051–11061. <https://doi.org/10.1002/2017GL074954>
- Mouginot, B.S. & Rignot, E. (2017) MEaSUREs Antarctic Boundaries for IPY 2007–2009 from Satellite Radar, Version 2. <https://doi.org/10.5067/AXE4121732AD>
- Mouginot, J., Rignot, E. & Scheuchl, B. (2019) Continent-wide, interferometric SAR phase, mapping of Antarctic ice velocity. *Geophysical Research Letters*, 46(16), 9710–9718. <https://doi.org/10.1029/2019GL083826>
- Mueller, C.O. & Jokat, W. (2019) The initial Gondwana break-up: A synthesis based on new potential field data of the Africa–Antarctica corridor. *Tectonophysics*, 750, 301–328. <https://www.sciencedirect.com/science/article/abs/pii/S0040195118303858>
- Näslund, J.O. (2001) Landscape development in western and central Dronning Maud Land, East Antarctica. *Antarctic Science*, 13(3), 302–311. <https://doi.org/10.1017/S0954102001000438>
- Nixdorf, U., Steinhage, D., Meyer, U., Hempel, L., Jenett, M., Wachs, P. & Miller, H. (1999) The newly developed airborne radio-echo sounding system of the AWI as a glaciological tool. *Annals of Glaciology*, 29, 231–238. <https://doi.org/10.3189/172756499781821346>
- Oerlemans, J. (2010) Numerical experiments on large scale glacial erosion. *Zeitschrift für Gletscherkunde und Glaziologie*, 20, 107–126.
- Pattyn, F. (2010) Antarctic subglacial conditions inferred from a hybrid ice sheet/ice stream model. *Earth and Planetary Science Letters*, 295(3), 451–461. <https://www.sciencedirect.com/science/article/pii/S0012821X10002712>
- Paxman, G.J.G., Gasson, E.G.W., Jamieson, S.S.R., Bentley, M.J. & Ferraccioli, F. (2020) Long-term increase in Antarctic ice sheet vulnerability driven by bed topography evolution. *Geophysical Research Letters*, 47(20), e2020GL090003. <https://agupubs.onlinelibrary.wiley.com/doi/abs/10.1029/2020GL090003>
- Riedel, S., Jokat, W. & Steinhage, D. (2012) Mapping tectonic provinces with airborne gravity and radar data in Dronning Maud Land, East Antarctica. *Geophysical Journal International*, 189(1), 414–427. <https://doi.org/10.1111/j.1365-246X.2012.05363.x>
- Rignot, E., Jacobs, S., Mouginot, J. & Scheuchl, B. (2013) Ice-shelf melting around Antarctica. *Science*, 341(6143), 266–270. <https://science.sciencemag.org/content/341/6143/266>
- Rippin, D.M., Bingham, R.G., Jordan, T.A., Wright, A.P., Ross, N., Corr, H.F. J. et al. (2014) Basal roughness of the Institute and Möller Ice Streams West Antarctica: Process determination and landscape interpretation. *Geomorphology*, 214, 139–147. <https://doi.org/10.1016/j.geomorph.2014.01.021>
- Rodriguez-Morales, F., Gogineni, S., Leuschen, C.J., Paden, J.D., Li, J., Lewis, C.C. et al. (2014) Advanced multifrequency radar instrumentation for polar Research. *IEEE Transactions on Geoscience and Remote Sensing*, 52(5), 2824–2842. <https://doi.org/10.1109/TGRS.2013.2266415>
- Rose, K.C., Ross, N., Jordan, T.A., Bingham, R.G., Corr, H.F.J., Ferraccioli, F. et al. (2015) Ancient pre-glacial erosion surfaces preserved beneath the West Antarctic Ice Sheet. *Earth Surface Dynamics*, 3(1), 139–152. <https://esurf.copernicus.org/articles/3/139/2015/>
- Ross, N., Bingham, R.G., Corr, H.F.J., Ferraccioli, F., Jordan, T.A., Le Brocq, A. et al. (2012) Steep reverse bed slope at the grounding line of the Weddell Sea sector in West Antarctica. *Nature Geoscience*, 5(6), 393–396. <https://doi.org/10.1038/ngeo1468>
- Ross, N., Jordan, T.A., Bingham, R.G., Corr, H.F.J., Ferraccioli, F., Le Brocq, A. et al. (2014) The Ellsworth Subglacial Highlands: Inception and retreat of the West Antarctic Ice Sheet. *GSA Bulletin*, 126(1–2), 3–15. <https://doi.org/10.1130/B30794.1>
- Shapiro, N.M. & Ritzwoller, M.H. (2004) Inferring surface heat flux distributions guided by a global seismic model: Particular application to Antarctica. *Earth and Planetary Science Letters*, 223(1), 213–224. <http://www.sciencedirect.com/science/article/pii/S0012821X0400247X>
- Shepard, M.K., Campbell, B.A., Bulmer, M.H., Farr, T.G., Gaddis, L.R. & Plaut, J.J. (2001) The roughness of natural terrain: A planetary and remote sensing perspective. *Journal of Geophysical Research: Planets*, 106(E12), 32777–32795. <https://doi.org/10.1029/2000JE001429>
- Shevenell, A.E., Kennett, J.P. & Lea, D.W. (2004) Middle Miocene Southern Ocean cooling and Antarctic cryosphere expansion. *Science*, 305(5691), 1766–1770. <https://science.sciencemag.org/content/305/5691/1766>
- Siegert, M.J., Taylor, J. & Payne, A.J. (2005) Spectral roughness of subglacial topography and implications for former ice-sheet dynamics in East Antarctica. *Global and Planetary Change*, 45(1–3), 249–263. <https://doi.org/10.1016/j.gloplacha.2004.09.008>
- Smith, E.C., Hattermann, T., Kuhn, G., Gaedicke, C., Berger, S., Drews, R. et al. (2020) Detailed seismic bathymetry beneath Ekström ice shelf, Antarctica: Implications for glacial history and ice–ocean interaction. *Geophysical Research Letters*, 47(10), e2019GL086187. <https://agupubs.onlinelibrary.wiley.com/doi/abs/10.1029/2019GL086187>
- Steinhage, D. (2001) *Beiträge aus geophysikalischen Messungen in Dronning Maud Land, Antarktis, zur Auffindung eines optimalen Bohrpunktes für eine Eiskerntiefbohrung*, Berichte zur Polar- und Meeresforschung, Vol. 384. Bremerhaven: Alfred-Wegener-Institut für Polar- und Meeresforschung.
- Steinhage, D., Nixdorf, U., Meyer, U. & Miller, H. (1999) New maps of the ice thickness and subglacial topography in Dronning Maud Land, Antarctica, determined by means of airborne radio-echo sounding. *Annals of Glaciology*, 29, 267–272. <https://doi.org/10.3189/172756499781821409>
- Sternai, P., Herman, F., Fox, M.R. & Castellort, S. (2011) Hypsometric analysis to identify spatially variable glacial erosion. *Journal of Geophysical Research: Earth Surface*, 116, F03001. <https://doi.org/10.1029/2010JF001823>
- Stroeven, A.P., Fabel, D., Hätttestrand, C. & Harbor, J. (2002) A relict landscape in the centre of fennoscandian glaciation: Cosmogenic radionuclide evidence of tors preserved through multiple glacial cycles. *Geomorphology*, 44(1), 145–154. <https://www.sciencedirect.com/science/article/pii/S0169555X01001507>
- Sugden, D.E. (1968) The selectivity of glacial erosion in the Cairngorm Mountains, Scotland. *Transactions of the Institute of British Geographers*, 45, 79–92. <http://www.jstor.org/stable/621394>

- Sugden, D.E. (1978) Glacial erosion by the Laurentide Ice Sheet. *Journal of Glaciology*, 20(83), 367–391. <https://doi.org/10.3189/S0022143000013915>
- Sugden, D.E., Denton, G.H. & Marchant, D.R. (1995) Landscape evolution of the Dry Valleys, Transantarctic Mountains: Tectonic implications. *Journal of Geophysical Research: Solid Earth*, 100(B6), 9949–9967. <https://agupubs.onlinelibrary.wiley.com/doi/abs/10.1029/94JB02895>
- Sugden, D.E. & Jamieson, S.S.R. (2018) The pre-glacial landscape of Antarctica. *Scottish Geographical Journal*, 134(3–4), 203–223. <https://doi.org/10.1080/14702541.2018.1535090>
- Sugden, D.E. & John, B.S. (1976) *Glaciers and Landscape: A Geomorphological Approach*, Vol. 365. London: Edward Arnold.
- Talalay, P., Li, Y., Augustin, L., Clow, G.D., Hong, J., Lefebvre, E. et al. (2020) Geothermal heat flux from measured temperature profiles in deep ice boreholes in Antarctica. *The Cryosphere*, 14(11), 4021–4037. <https://tc.copernicus.org/articles/14/4021/2020/>
- Thomson, S.N., Brandon, M.T., Tomkin, J.H., Reiners, P.W., Vásquez, C. & Wilson, N.J. (2010) Glaciation as a destructive and constructive control on mountain building. *Nature*, 467(7313), 313–317. <https://doi.org/10.1038/nature09365>
- Van Liefferinge, B., Pattyn, F., Cavitte, M.G.P., Karlsson, N.B., Young, D.A., Sutter, J. & Eisen O. (2018) Promising oldest ice sites in East Antarctica based on thermodynamical modelling. *The Cryosphere*, 12(8), 2773–2787. <https://tc.copernicus.org/articles/12/2773/2018/>
- Wang, C.-C., Jacobs, J., Elburg, M.A., Läufer, A. & Elvevold, S. (2020) Late Neoproterozoic–Cambrian magmatism in Dronning Maud Land (East Antarctica): U–Pb zircon geochronology, isotope geochemistry and implications for Gondwana assembly. *Precambrian Research*, 350, 105880. <https://doi.org/10.1016/j.precamres.2020.105880>
- Weikusat, I., Jansen, D., Binder, T., Eichler, J., Faria, S.H., Wilhelms, F. et al. (2017) Physical analysis of an Antarctic ice core: Towards an integration of micro- and macrodynamics of polar ice. *Philosophical Transactions of the Royal Society A: Mathematical, Physical and Engineering Sciences*, 375(2086), 20150347. <https://doi.org/10.1098/rsta.2015.0347>
- Wilhelms, F., Miller, H., Gerasimoff, M.D., Drücker, C., Frenzel, A., Fritzsche, D. et al. (2014) The EPICA Dronning Maud Land deep drilling operation. *Annals of Glaciology*, 55(68), 355–366. <https://doi.org/10.3189/2014AoG68A189>
- Winter, A., Steinhage, D., Arnold, E.J., Blankenship, D.D., Cavitte, M.G.P., Corr, H.F.J. et al. (2017) Comparison of measurements from different radio-echo sounding systems and synchronization with the ice core at dome C, Antarctica. *The Cryosphere*, 11(1), 653–668. <https://tc.copernicus.org/articles/11/653/2017/>
- Young, D.A., Wright, A.P., Roberts, J.L., Warner, R.C., Young, N.W., Greenbaum, J. S. et al. (2011) A dynamic early East Antarctic Ice Sheet suggested by ice-covered fjord landscapes. *Nature*, 474(7349), 72–75. <https://doi.org/10.1038/nature10114>
- Zimmer, P.D. & Gabet, E.J. (2018) Assessing glacial modification of bedrock valleys using a novel approach. *Geomorphology*, 318, 336–347. <https://www.sciencedirect.com/science/article/pii/S0169555X18302526>

How to cite this article: Franke, S., Eisermann, H., Jokat, W., Eagles, G., Asseng, J., Miller, H. et al. (2021) Preserved landscapes underneath the Antarctic Ice Sheet reveal the geomorphological history of Jutulstraumen Basin. *Earth Surface Processes and Landforms*, 46(13), 2728–2745. <https://doi.org/10.1002/esp.5203>